Theses and Dissertations   1. Thesis and Dissertation Collection, all items

2007-03

Characteristics and use of a nonlinear end-fired array for acoustics in air

Akar, Ali Onur

Monterey California. Naval Postgraduate School

http://hdl.handle.net/10945/3637

NAVAL
POSTGRADUATE
SCHOOL

MONTEREY, CALIFORNIA

THESIS

CHARACTERISTICS AND USE OF A NONLINEAR END-FIRED ARRAY FOR ACOUSTICS IN AIR

by

Ali Onur Akar

March 2007

Co-Advisors: Andrés Larraza
                                     Bruce C. Denardo

Approved for public release; distribution is unlimited

THIS PAGE INTENTIONALLY LEFT BLANK

REPORT DOCUMENTATION PAGE		*Form Approved OMB No. 0704-0188*
Public reporting burden for this collection of information is estimated to average 1 hour per response, including the time for reviewing instruction, searching existing data sources, gathering and maintaining the data needed, and completing and reviewing the collection of information. Send comments regarding this burden estimate or any other aspect of this collection of information, including suggestions for reducing this burden, to Washington headquarters Services, Directorate for Information Operations and Reports, 1215 Jefferson Davis Highway, Suite 1204, Arlington, VA 22202-4302, and to the Office of Management and Budget, Paperwork Reduction Project (0704-0188) Washington DC 20503.		

1. AGENCY USE ONLY *(Leave blank)*	2. REPORT DATE March 2007	3. REPORT TYPE AND DATES COVERED Master's Thesis	
4. TITLE AND SUBTITLE: Characteristics and Use of a Parametric End-Fired Array for Acoustics in Air		**5. FUNDING NUMBERS**	
6. AUTHOR: Ali Onur Akar			
7. PERFORMING ORGANIZATION NAME AND ADDRESS Naval Postgraduate School Monterey, CA 93943-5000		**8. PERFORMING ORGANIZATION REPORT NUMBER**	
9. SPONSORING /MONITORING AGENCY NAME(S) AND ADDRESS(ES) N/A		**10. SPONSORING/MONITORING AGENCY REPORT NUMBER** N/A	
11. SUPPLEMENTARY NOTES The views expressed in this thesis are those of the author and do not reflect the official policy or position of the Department of Defense or the U.S. Government.			
12a. DISTRIBUTION / AVAILABILITY STATEMENT Approved for public release; distribution is unlimited		**12b. DISTRIBUTION CODE**	

13. ABSTRACT

The parametric array exploits two highly collimated ultrasound beams interacting in a given volume producing a single beam with very high directivity and almost no side lobes. The high directivity of the difference frequency signal of the parametric array is due to the interaction of the waves in the volume effectively producing a virtual end-fired array boosting pressure levels along the interaction region which is limited by the absorption coefficient. This thesis focuses on experiments conducted in an anechoic room using AS-18-B Audio Spotlight system from Holosonic^{TM}. Furthermore, nonlinear theory was modeled by a linear discrete array. The beam pattern of the parametric loudspeaker, range dependence of primary and secondary signals and total harmonic distortion (THD) were measured and then compared to theory. Experimental data for the beam pattern of the parametric loudspeaker agreed with the theory. It was all shown that the parametric array had a very narrow beam width and almost no side lobes as opposed to conventional loudspeakers. Both primary waves and difference wave frequency signals were examined for their range dependence. Due to the complicated interference of the primary waves, it was impossible to compare experimental results with theoretical predictions. For the difference wave signals, experimental data was verified by theory, which was modified in order to accommodate both wave generation and spreading region. Finally, THD of the parametric loudspeaker was measured for different amplitude modulation depths. Experimental results showed that preprocessing should be applied in order to decrease THD and achieve clean audio signal reproduction.

14. SUBJECT TERMS Parametric array, wave wave interaction, audio spotlight, sound scattering, nonlinear acoustics, ultrasound			**15. NUMBER OF PAGES** 81
			16. PRICE CODE
17. SECURITY CLASSIFICATION OF REPORT Unclassified	**18. SECURITY CLASSIFICATION OF THIS PAGE** Unclassified	**19. SECURITY CLASSIFICATION OF ABSTRACT** Unclassified	**20. LIMITATION OF ABSTRACT** UL

THIS PAGE INTENTIONALLY LEFT BLANK

CHARACTERISTICS AND USE OF A NONLINEAR END-FIRED ARRAY FOR ACOUSTICS IN AIR

Ali Onur Akar
Lieutenant Junior Grade, Turkish Navy
B.S., Turkish Naval Academy, 2002

Submitted in partial fulfillment of the
requirements for the degree of

MASTER OF SCIENCE IN ENGINEERING ACOUSTICS

from the

NAVAL POSTGRADUATE SCHOOL
March 2007

Author: Ali Onur Akar

Approved by: Andrés Larraza
                     Co-Advisor

                     Bruce C. Denardo
                     Co-Advisor

                     Kevin B. Smith, Chairman
                     Engineering Acoustics Academic Committee

iii

THIS PAGE INTENTIONALLY LEFT BLANK

ABSTRACT

The parametric array exploits two highly collimated ultrasound beams interacting in a given volume producing a single beam with very high directivity and almost no side lobes. The high directivity of the difference frequency signal of the parametric array is due to the interaction of the waves in the volume effectively producing a virtual end-fired array boosting pressure levels along the interaction region which is limited by the absorption coefficient. This thesis focuses on experiments conducted in an anechoic room using AS-18-B Audio Spotlight system from Holosonic^{TM}. Furthermore, nonlinear theory was modeled by a linear discrete array. The beam pattern of the parametric loudspeaker, range dependence of primary and secondary signals and total harmonic distortion (THD) were measured and then compared to theory. Experimental data for the beam pattern of the parametric loudspeaker agreed with the theory. It was also shown that the parametric array had a very narrow beam width and almost no side lobes as opposed to conventional loudspeakers. Both primary waves and difference wave frequency signals were examined for their range dependence. Due to the complicated interference of the primary waves, it was impossible to compare experimental results with theoretical predictions. For the difference wave signals, experimental data was verified by theory, which was modified in order to accommodate both wave generation and the spreading region. Finally, THD of the parametric loudspeaker was measured for different amplitude modulation depths. Experimental results showed that preprocessing should be applied in order to decrease THD and achieve clean audio signal reproduction.

THIS PAGE INTENTIONALLY LEFT BLANK

TABLE OF CONTENTS

THIS PAGE INTENTIONALLY LEFT BLANK

LIST OF FIGURES

x

LIST OF TABLES

THIS PAGE INTENTIONALLY LEFT BLANK

ACKNOWLEDGMENTS

THIS PAGE INTENTIONALLY LEFT BLANK

I.   INTRODUCTION

Most acoustic field applications can be modeled very accurately with linear models due to the fact that the amplitude of the sound waves is so small, but there are some applications where the linear acoustic field fails due to the high amplitude of the acoustic wave (Atchley, 2005). One of the important principles in nonlinear acoustics is that finite amplitude waves distort when they travel. This phenomenon is called *wave steepening* (Figure 1). The wave steepening process results in harmonic generation when a single frequency wave travels. It tends to become a sawtooth wave (Denardo & Larraza, 2006).
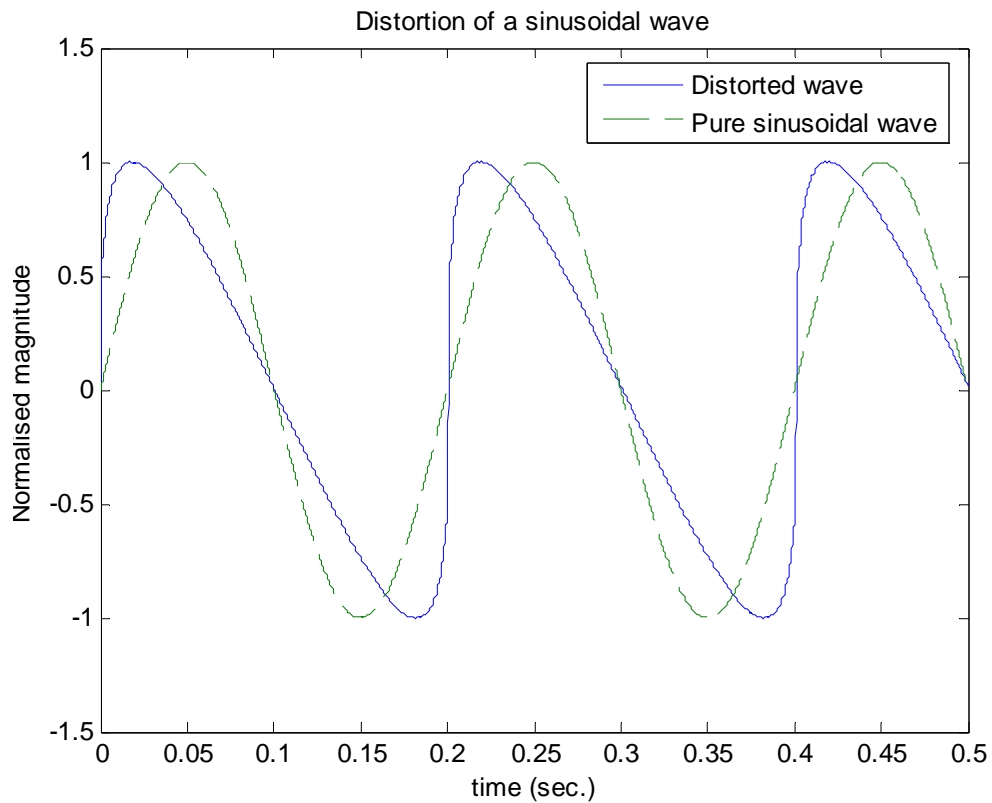
Figure 1.   Wave steepening. Illustration of linear and nonlinear theory, dotted line represents the single pure frequency while the continuous line represents the steepened wave due to the nonlinear effects. It tends to become a sawtooth wave.

If two different finite amplitude dispersionless sound waves are excited, there will be a significant interaction between them in the medium provided that the waves are collinear.

Linear theory says that the result of two sound waves is just a superposition of the individual waves alone. No additional frequency components are produced in linear theory. However, nonlinear interactions cause additional harmonics, as well as sum and difference waves to be produced in the medium. The parametric array exploits two highly collimated ultrasound beams interacting in the volume, producing a beam with very high directivity and almost no side lobes. The high directivity of the difference frequency of the parametric array is due to the interaction of the waves in the volume effectively producing a virtual end-fired array boosting pressure levels along the interaction region which is limited by the absorption coefficient.

A.   HISTORY OF PARAMETRIC ARRAYS

Parametric arrays have been used for long time in many different applications. The origin of the parametric arrays dates back to the 1960s as a sonar application for underwater use. The vast majority of the research for parametric arrays was devoted to underwater applications until the 1980s.

The theoretical explanation of the parametric arrays was first proposed by Westervelt (1963). He derived the directivity function of the secondary wave which is known as *Westervelt directivity function* and showed that collinear nonlinear interaction of plane waves produces sum and difference frequencies. His calculations were based on a quasilinear approach. Before the Westervelt theoretical analysis, the parametric array had already been demonstrated experimentally both in water and in air by Bellin and Beyer (1962). The results agreed well with the theory of Westervelt's scattering of sound by sound (1957). The only problem the researchers encountered was that they couldn't get enough data points due to the operating limitations. While they could only get three valid data points, these agreed well with Westervelt predictions. More detailed work was carried out both experimentally and theoretically by Berktay (1965) in the following years. He extended Westervelt's derivations and included the conditions of primary wave

cylindrical and spherical spreading. Berktay also concluded that parametric arrays can be used for low-frequency sector-scanning arrays, and also for the calibration of hydrophones and receivers for wide band sonar. All of the researchers mentioned above mainly focused their efforts on parametric arrays for underwater applications, because at that time it was not believed that the parametric arrays would work in air. Benneth and Blackstock (1975) successfully developed a parametric array in air by using a circular piston transducer. They observed that a 5 kHz difference wave had narrow beam width, with side-lobe-free beam pattern in their experiment, by exciting the transducer with 18.6 kHz and 23.6 kHz primary frequencies. After it was proved that parametric arrays also work in air, many researchers were attracted to develop a parametric loudspeaker for audio production. The first parametric loudspeaker for audio production was invented by Yoneyama, Fujimoto, Kawamo, and Sasabe (1983). The parametric loudspeaker array that they have invented consisted of 547 PZT bimorph transducers with resonance at about 40 kHz (Figure 2).

Yoneyama et al. (1983) amplitude modulated the ultrasound with an audio signal. Due to nonlinear effects, the audio signal is generated in the air and self-demodulates. However, the produced sound pressure field has an ω^2 dependence. Therefore, they suggested that in order to get flat response an equalizer should be used in the experiment. However, the biggest problem they faced was the harmonic distortion due to nonlinear effects[1].

Total harmonic distortion (THD) is an important issue for high fidelity music reproduction. This problem was solved by Pompei (1999) by using the preprocessing scheme that was developed by Kite, Post, Hamilton (1998). Pompei (1999) designed the first parametric loudspeaker that has the capability of broadband spectrum and high fidelity audio. In our experiment, we are using the parametric speaker that he developed and marketed for Holosonics Company (Figure 3). Pompei managed to reduce the THD below 5% for most of the low frequency audio spectrum.

---

[1] See Chapter II for the theory of demodulation.

Figure 2.   The first parametric loudspeaker from Yoneyama, et al. (1983).

4

Figure 3.   The Audio Spotlight developed by Pompei.

B.   APPLICATIONS OF PARAMETRIC ARRAYS

The parametric arrays have been used extensively because of their unique features, which include very high directivity at low frequencies without unwanted side lobes. They are generally used as a wide band sonar system for direct measurement of environmental parameters in shallow waters, in fisheries, and in bottom area sounding when the reverberation is a problem (Naugolnykh & Ostrovsky, 1998; Hines, Risley & O'Connor, 1998). Having a beam pattern with significantly reduced side lobes, as is the case of the parametric array, prevents interference due to the boundary interactions in shallow waters. Parametric arrays can also be used in sub-bottom and seismic profiling due to its high resolution features (Muir & Wyber, 1984). They have some advantages over conventional transducers in calibration of hydrophones because with only one single transducer, wide band frequency can be achieved while narrow beam pattern and short pulses provide reduction in boundary reflection problems (Konrad & Navin, 1973).

In addition to underwater use, parametric arrays have been used in different applications in the air. For instance, parametric loudspeakers have been used widely since 2000 in a variety of places like museums, airports, offices, galleries etc. as an audio

spotlight. There is also some study for the possible use of parametric arrays for detecting buried mines and chemical waste in the soil (Wijk, Scales, Mikesell & Peacock, 2005).

C.   SCOPE OF THE THESIS AND OUTLINE

This thesis focuses on experiments conducted in an anechoic room by using AS-18-B Audio spotlight from Holosonics. These experiments, conducted only in air, will enable a better understanding of the parametric arrays. The experimental results are compared with the theory from Westervelt (1963). Furthermore the nonlinear theory will be attempted to be mimicked by a linear array.

In Chapter II, a theoretical background of scattering of sound by sound and parametric array transmitters and receivers is investigated thoroughly. Westervelt's equation and Berktay's approach are introduced and compared.

Chapter III describes the linear array theory and beam pattern of the conventional end-fired arrays in detail. In this chapter parametric end-fired array is modeled by linear end-fired array. Beam patterns of different interaction length are compared.

Chapter IV presents the experimental results conducted with the Audio Spotlight in the NPS anechoic room. The beam pattern of the loudspeaker, range dependence of the primary and secondary signals and total harmonic distortion are measured and then compared by the theory.

Finally, Chapter V summarizes the thesis, presents conclusions, and discusses future work.

II.   THEORY OF PARAMETRIC ARRAYS

A.   THEORY OF PARAMETRIC ARRAYS

Nonlinear interaction of two collinear and highly collimated intense sound beams can create harmonics as well as sum and difference frequencies due to the nonlinearity of the medium in the fluid equations. If we define the primary frequencies as ω_1 and ω_2, the generated frequencies in the medium would be in the combination,

$$n\omega_1 \pm m\omega_2 \quad . \tag{2.1}$$

We will follow the approach by Westervelt, which is a quasilinear theory. "Quasilinear" in this context means that due to nonlinearity, the second-order perturbation of the primary frequency waves will drive a second-order wave which propagates according to linear theory. There will thus be acoustic propagation for the sum, difference and primary frequency waves. Of interest to us are ultrasonic waves where the frequencies of the primary waves are nearly equal ($\omega_1 \approx \omega_2$), so that the difference frequency product is a low frequency field. The low frequency field can also be created by amplitude modulation. For instance, if a 60 kHz ultrasonic frequency signal is amplitude modulated by a 2 kHz audio signal, the result is

$$y(t) = [1 + m\cos(\omega_s t)]\cos(\omega_p t) , \tag{2.2}$$

where ω_s is the audio signal, ω_p is ultrasonic frequency and m is the modulation depth that controls the amplitude of the modulation. Figure 4 shows the signal for a modulation depth of unity. In the frequency domain there is energy in the upper sideband of 62 kHz, the lower sideband of 58 kHz, and the 60 kHz carrier signal. Due to nonlinear interaction, the carrier signal (ω_p) and lower and upper sidebands generate a low frequency field (audible). There will also be interaction between the sidebands which causes the harmonic distortion because interaction between side bands generates a second harmonic of the desired difference frequency wave.

The modulation depth can be varied between 0 and 1. Decreasing the modulation depth results in reduction of the sound pressure level for the difference wave because the

sound pressure of the difference wave is proportional to *2m*. On the other hand, reducing *m* will decrease the total harmonic distortion (THD) for the audible field since THD is proportional to m^2.
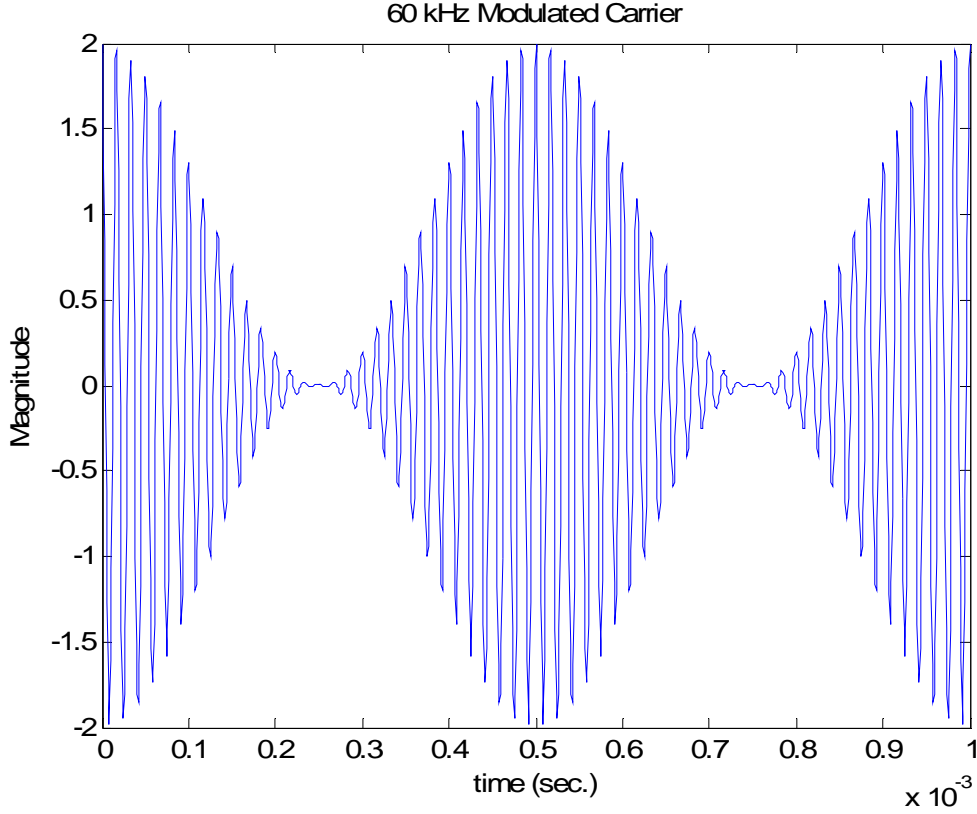
Figure 4.   Modulated 60 kHz signal with 2 kHz audio signal and modulation depth equal to one.

The primary frequency and the sum frequency waves decay rapidly because of the high absorption rates, while the difference frequency wave propagates long distances. Absorption plays a significant role and it is the reason devices bases on this principle are called parametric end-fired arrays. Along the interaction length, which is determined by the absorption of the ultrasonic frequencies, nonlinearities will add in phase like a linear end-fired array and produce a difference frequency wave. The primary waves are confined by the surface of the aperture because it is assumed that the primary waves are highly collimated. Exponential tapering due to the absorption of ultrasonic frequencies causes the side lobes to disappear in the parametric array. Thus, along the interaction length it is as though virtual point sources which are the result of nonlinear interaction of

8

ultrasonic frequency waves make up a virtual end-fired array as depicted in Fig. 5. The longer the array length, the higher the sound pressure can be achieved from the end-fired array. Thus, absorption determines the length of the array. Accordingly, the interaction length of the parametric arrays can be computed as

$$L = \frac{1}{2\alpha} \tag{2.3}$$

where α is the absorption coefficient of the ultrasonic frequency wave. This distance may be in the near field or in the far field of the aperture according to the primary frequencies used in the application.

Another factor that limits the length of the array is harmonic distortion and shock formation. As the transmitted power is increased, it may cause the primary waves to form shocks. This mechanism limits the difference frequency wave generation.
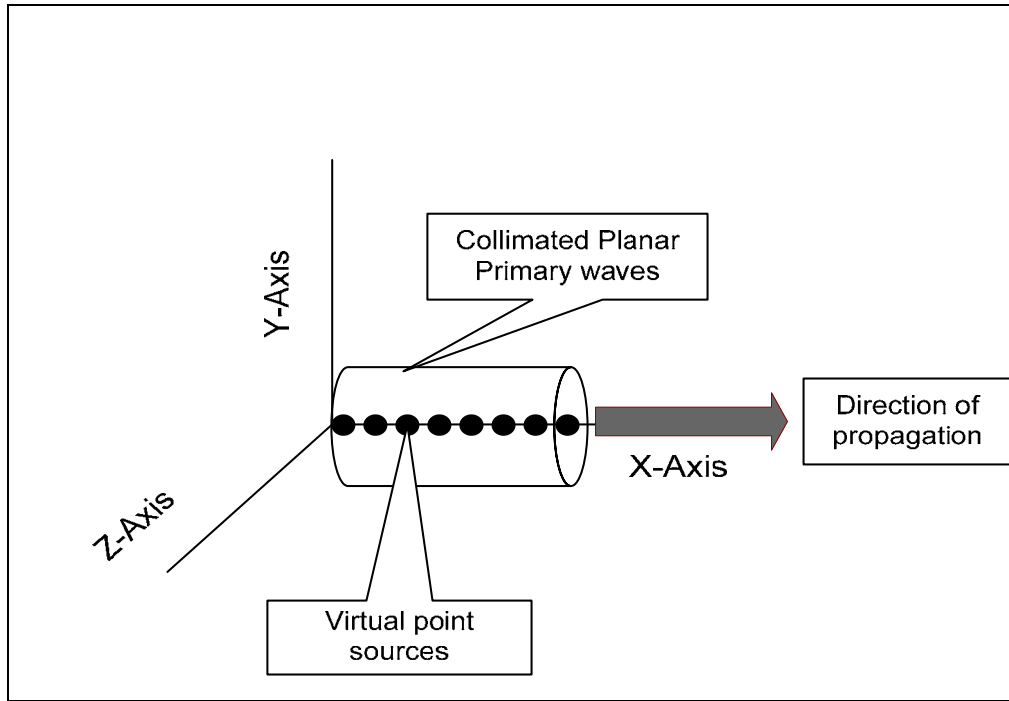
Figure 5.   Parametric end-fired array geometry by the collimated plane waves.

There are three main advantages of the parametric end-fired array. First, by using small transducers very high directivity can be achieved at low frequencies. Second, due to absorption, the difference frequency wave is nearly free of side lobe beam patterns.

9

Finally, the parametric end-fired array exhibits broadband capability at low frequencies. These unique features have allowed parametric end-fired arrays to be used in a variety of applications. One of the main problems in the parametric arrays is the conversion inefficiency. High power outputs are limited by saturation and absorption. Therefore the output from parametric end-fired array is limited (Vyas, Raj & Gupta, 1998). The other problem in the parametric end-fired array is the harmonic distortion, but by using preprocessing techniques total harmonic distortion (THD) has been reduced to below 5% from 30% in the recent years.

B.   WAVE –WAVE INTERACTION

In linear acoustics, due to the superposition principle, two waves will create contributions from each individual waves. There is no interaction and no additional harmonics will be created, as opposed to nonlinear case where energy of a harmonic disturbance from a pure signal generates new harmonics (Figure 6).
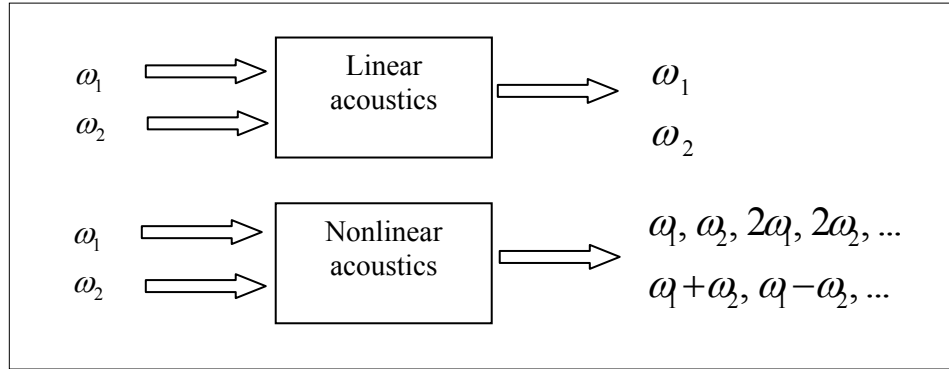
Figure 6.   Representation of harmonic frequency generation in nonlinear acoustics.

In nonlinear acoustics, two sound waves of frequencies ω_1 and ω_2 propagating in the same direction cause scattered sound waves outside of the interaction region, including second-order waves with frequencies $\omega_1 \pm \omega_2$. Interacting sound waves at other than zero angles do not cause scattered wave outside the interaction region. These results were shown theoretically by Westervelt (1957) and experimentally by Bellin and Beyer (1960). According to the Westervelt theory, if two perfectly collimated sound beams

interact at right angles, no scattering is expected outside the interaction region. Westervelt had also stated that an arbitrary interaction angle other than zero does not cause scattering.

The starting point for the calculations of scattered wave field is Lighthill's exact wave equation

$$\frac{\partial^2 \rho}{\partial t^2} - c_0^{\,2} \nabla^2 \rho = \frac{\partial^2 T_{ij}}{\partial x_i \partial x_j} \quad , \tag{2.4}$$

where ρ is the density of the medium, c_0 is the velocity of the sound speed in the medium and T_{ij} is the stress tensor, defined as

$$T_{ij} = \rho u_i u_j + p_{ij} - c_0^{\,2} \rho \delta_{ij} \quad . \tag{2.5}$$

The first term at the right side of the Eq. (2.5) is the Reynold's stress tensor, p_{ij} is the normal component of the pressure (compressive stress tensor) and δ_{ij} is the Kronecker delta function. The fluid is assumed to be ideal and homogenous, for which the ambient density and ambient pressure are both constant. The acoustic pressure can be found from the barotropic equation of state

$$p = c_0^{\,2} \rho + \sum_{n=2}^{\infty} \frac{1}{n!} \left(\frac{d^2 p}{d\rho^2} \right)_{\rho = \rho_0} \rho^n \tag{2.6}$$

To second order, the stress tensor yields

$$T_{ij} = \rho_0 u_i u_j + \frac{1}{2} \left(\frac{d^2 p}{d\rho^2} \right)_{\rho = \rho_0} \rho^2 \delta_{ij} \tag{2.7}$$

Interactions between sound waves causes stress tensor to form in the interaction region and that drives the linear equation as a source term. The sound waves should interact at zero angle and they should be highly collimated in order to exist outside the interaction region. Substituting Eq. (2.7) into Eq. (2.4) yields

11

$$\nabla^2 \rho_s - \frac{1}{c_0^{\,2}}\left(\frac{\partial^2 \rho_s}{\partial t^2}\right) = -\frac{1}{c_0^{\,2}}\frac{\partial^2}{\partial x_i \partial x_j}\left[\rho_0 u_i u_j + \frac{1}{2}\left(\frac{d^2 p}{d\rho^2}\right)_{\rho=\rho_0}\rho^2 \delta_{ij}\right] \qquad (2.8)$$

The right side of this equation is the source function that drives the secondary field. After this point we are going to define $\nabla^2 - \dfrac{1}{c_0^{\,2}}\dfrac{\partial^2}{\partial t^2} = \Box$, and it is called d'Alembertian operator.

By introducing energy density functions,

$$\text{Kinetic energy density} = T = \frac{1}{2}\rho_0 u^2$$

$$\text{Potential energy density} = V = \frac{1}{2}c_0^{\,2}\rho_0^{\,-1}\rho^2 \qquad (2.9)$$

$$\text{Total energy density} = E = V + T \,,$$

Eq. (2.8) can be written in more compact form

$$\Box \rho_s = c_0^{\,-2}\left\{\Box E - \nabla^2\left[2T + \rho_0 c_0^{\,-2}\left(\frac{d^2 p}{d\rho^2}\right)_{\rho=\rho_0} V\right]\right\} \qquad (2.10)$$

From this equation it can be seen that right side of the equation goes to zero when d'Alembertian of the energy density equals the Laplacian of the kinetic energy plus the potential energy. When that situation occurs, no scattered wave is generated outside the interaction region because we end up with a linear homogenous wave equation that has no source term included. Since the energy density (E) is always zero outside the interaction region, the Laplacian term will be effective for creation of scattered waves outside the interaction region. Therefore if the Laplacian term is also to zero, there will not be a scattered wave outside the interaction region. This situation occurs when:

$$T = -\frac{1}{2}\rho_0 c_0^{\,-2}\left(\frac{d^2 p}{d\rho^2}\right)_{\rho=\rho_0} V \qquad (2.11)$$

12

If we define the interaction potential energy for two waves interacting at an arbitrary angle as

$$T = \cos(\theta)V \tag{2.12}$$

Equation (2.11) becomes

$$\cos(\theta) = -\frac{1}{2}\rho_0 c_0^{-2}\left(\frac{d^2 p}{d\rho^2}\right)_{\rho=\rho_0}. \tag{2.13}$$

From Eq. (2.13) the angle of intersection of two sound waves can be computed for which there will be no scattered waves outside of the interaction region. This value is about 104º for air and 90º for liquids (Westervelt, 1957). Equation (2.13) was first derived by Westervelt. It indicates that two mutually perpendicular sound waves that interact with each other in the air do not produce a scattered wave outside the interaction region. In addition to this theory, Westervelt and later Bellin showed in their experiment that any sound waves interacting with each other at an arbitrary angle do not produce scattered waves outside the interaction region as long as the waves are not collinear.

C.   PARAMETRIC ARRAY TRANSMITTERS

If two high-frequency waves are produced by a single rectangular or circular piston source, they can be assumed to be highly collimated and to satisfy the conditions for interaction according to the Westervelt theory. In this case, the volume distribution of the point sources, which are the result of nonlinear interaction, can be thought as a line distribution on the acoustic axis of the piston source. This condition is only true if the area of the beam is negligible compared to the wavelength square of the ultrasonic frequency (Berktay, 1965). Under these conditions, the directivity of the source does not have any effect on the directivity of the difference wave. Otherwise, the directivity of the source should be taken into account and multiplied by the Westervelt directivity function. The derivation of the Westervelt directivity function will be done in the following section.

There are two different methods of generation of the difference frequency in the medium. Both methods will be investigated theoretically, because of their relevance to

applications of the parametric arrays. One method addresses excitation with two ultrasonic frequencies and the other method deals with amplitude modulation of the ultrasonic frequency by audio frequency which the medium demodulates due to nonlinear effects. The latter method is used in audio applications for loudspeakers. In Chapter IV we report measurements on a loudspeaker based on this latter method.

1. Westervelt Approach

Consider a piston source that excites simultaneously two close ultrasonic frequencies ω_1 and ω_2. A difference frequency ($\omega_1 - \omega_2$) signal within audible range and sum frequency ($\omega_1 + \omega_2$) signal outside the audible range will be produced. The two primary waves can be defined as

$$
\begin{aligned}
P_1 &= P_0 e^{-\alpha x} \cos(\omega_1 t - k_1 x) \\
P_2 &= P_0 e^{-\alpha x} \cos(\omega_2 t - k_2 x)
\end{aligned}
\tag{2.14}
$$

which for now we consider to be of the same amplitude. Following Westervelt (1963) we assume that the primary waves are collinear, perfectly collimated, and narrow plane waves. Furthermore, absorption of the secondary difference wave is negligible and the primary waves can be assumed to have the same absorption coefficient because their frequencies are nearly equal.

The Westervelt (1963) equation in this case reduces to

$$
\nabla^2 p_d - \frac{1}{c_0^2} \frac{\partial^2 p_d}{\partial t^2} = -\rho_0 \frac{\partial q}{\partial t}, \qquad q = \frac{\beta}{\rho_0^2 c_0^4} \frac{\partial}{\partial t} p_i^2
\tag{2.15}
$$

where p_i is the primary wave and the p_d is the difference wave. q is the source strength that drives the difference wave. Since the calculations are based on the quasilinear approach, perturbation expansions up to a second order need to be used. The perturbation method consists in power series by a small parameter correction which is the deviation from the linear solution

$$
p = p_1 + \varepsilon p_2 + \varepsilon^2 p_3 + \dots
\tag{2.16}
$$

where p is the acoustic pressure, p_1 is the solution to linear equation and p_2 is the second order correction term to linear theory. Since the interaction should be collinear, the difference wave should be unidirectional. Assuming propagation is in the x direction, the first order linear approximation of wave equation is then:

$$\frac{\partial^2 p_1}{\partial x^2} - \frac{1}{c_0^2}\frac{\partial^2 p_1}{\partial t^2} = 0. \tag{2.17}$$

At the second order we get:

$$\nabla^2 p_2 - \frac{1}{c_0^2}\frac{\partial^2 p_2}{\partial t^2} = \frac{\beta}{\rho_0 c_0^4}\frac{\partial^2 p_1^2}{\partial t^2}. \tag{2.18}$$

Equation (2.18) can be interpreted as point sources that are distributed continuously along the interaction length. The right side of the Eq. (2.18) is called source strength density and β is the coefficient of nonlinearity

$$\beta = 1 + \frac{B}{2A} \tag{2.19}$$

where B/A is the nonlinearity of the medium, where

$$A = \frac{\rho_0}{p_0}c_0^2 \quad \text{and} \quad B = \frac{\rho_0^2}{p_0}\left(\frac{\partial^2 p}{\partial \rho^2}\right)_{\rho=\rho_0}. \tag{2.20}$$

Some of the important properties of the air which is used frequently in the equations are listed at the Table 1.

Temperature (°C)	Sound velocity c_0 (m/s)	Density ρ_0 (kg/m³)	Nonlinearity parameter β	Characteristic Impedance $\rho_0 c_0$ (Pa.s/m)
20°C	343	1.21	1.2	415

Table 1.   Properties of air (Kinsler, Frey, Coppens & Sanders, 2000).

15

Nonhomogenous differential equations can be solved by using Green's function. Therefore in order to calculate the difference frequency wave field, Equation (2.18) can be solved via time-independent free-space Green's function, where the geometry is shown in Fig.7:

$$g_f(r,r_0) = -\frac{e^{-ik|r-r_0|}}{4\pi|r-r_0|} \tag{2.21}$$
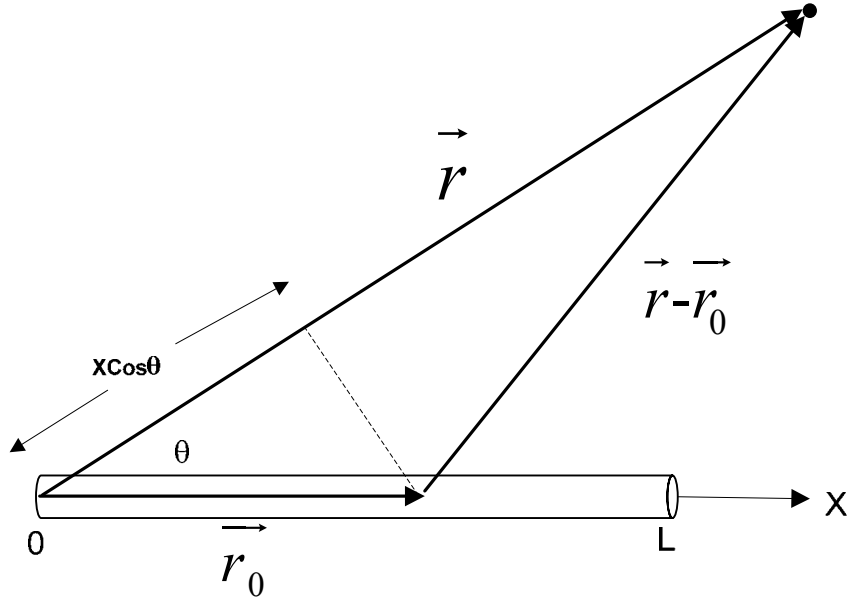
Figure 7. Geometry of the parametric array problem [After (Westervelt, 1963)].

By taking the volume integral of the inhomogeneous linear wave Equation (2.18) and substituting Eq. (2.21) into the integral:

$$p_d(r) = -\frac{1}{4\pi}\int \frac{\beta}{\rho_0 c_0^4}\frac{\partial^2}{\partial t^2}p_i^2\frac{e^{-ik|r-r_0|}}{|r-r_0|}dV, \tag{2.22}$$

one gets the solution to a wave equation for the secondary field that is made up from the contributions of the primary field. Squaring primary waves from Eq. (2.14) and substituting into the Eq. (2.22) yields

$$P_0^2 e^{-2\alpha x}\left[\cos^2(\omega_1 t - k_1 x) + \cos^2(\omega_2 t - k_2 x) + 2\cos(\omega_1 t - k_1 x)\cos(\omega_2 t - k_2 x)\right]. \tag{2.23}$$

16

First two terms in the parentheses contribute nothing for the difference wave ($\omega_1 - \omega_2$); they contribute to the second harmonic for primary waves ($2\omega_1, 2\omega_2$). Therefore we ignore these first two and use the a trigonometry identity for the third term in the parenthesis, to obtain

$$P_0^2 e^{-2\alpha x}\left\{\cos\left[(\omega_1 + \omega_2)t - (k_1 + k_2)x\right] + \cos\left[(\omega_1 - \omega_2)t - (k_1 - k_2)x\right]\right\}. \qquad (2.24)$$

For our purposes we are only dealing with the difference wave and thus we can also ignore the first term in Eq. (2.24). Taking the second derivative with respect to time and substituting it into Eq. (2.22) we end up with:

$$p_d(r) = -\frac{1}{4\pi}\int \frac{\beta P_0^2 e^{-2\alpha x}\omega_d^2 \cos(\omega_d t - k_d x)}{\rho_0 c_0^4}\frac{e^{-ik_d|r - r_0|}}{|r - r_0|}dV. \qquad (2.25)$$

The cosine term in Eq. (2.25) can be written in the complex form, which makes the integral simpler to solve.

$$p_d(r) = -\frac{1}{4\pi}\int \frac{\beta P_0^2 e^{-2\alpha x}\omega_d^2 e^{i(\omega_d t - k_d x)}}{\rho_0 c_0^4}\frac{e^{-ik_d|r - r_0|}}{|r - r_0|}dV. \qquad (2.26)$$

Using a far field approximation and the geometry in Fig. 6, Eq. (2.26) can be simplified to

$$p_d(r,\theta) = -\frac{1}{4\pi}\int \frac{P_0^2 e^{-2\alpha x}\omega_d^2 e^{i(\omega_d t - k_d x)}}{\rho_0 c_0^4}\frac{e^{-ik_d(r - x\cos(\theta))}}{r}dV. \qquad (2.27)$$

This volume integral can be simplified to one dimension by using the elementary volume of the source density $S_0 dx$

$$p_d(r,\theta) = -\frac{1}{4\pi}\int_0^l \frac{S_0\beta P_0^2 e^{-2\alpha x}\omega_d^2 e^{i(\omega_d t - k_d x)}}{\rho_0 c_0^4}\frac{e^{-ik_d(r - x\cos(\theta))}}{r}dx \qquad (2.28)$$

where l is the interaction length and S_0 is the surface area of the aperture:

$$p_d(r,\theta) = -\frac{S_0\beta P_0^2 \omega_d^2 e^{i\omega_d t}e^{-ik_d r}}{4\pi\rho_0 c_0^4 r}\int_0^l e^{ix(-k_d + 2i\alpha + k_d\cos(\theta))}dx. \qquad (2.29)$$

When $\alpha\ell >> 1$, upper limit for the integral in Eq. (2.29) can be evaluated as:

$$p_d(r,\theta) = -\frac{S_0\beta P_0^2\omega_d^2 e^{i\omega_d t}e^{-ik_d r}}{4\pi\rho_0 c_0^4 r}\left[\frac{e^{ix(-k_d+2i\alpha+k_d\cos(\theta))}}{i(-k_d+2i\alpha+k_d\cos(\theta))}\right]_0^\infty \tag{2.30}$$

$$= \frac{S_0\beta P_0^2\omega_d^2 e^{i\omega_d t}e^{-ik_d r}}{4\pi\rho_0 c_0^4 r}\left[\frac{1}{ik_d(-1+\cos(\theta))-2\alpha}\right]. \tag{2.31}$$

By using trigonometric identities, Eq. (2.31) can be written:

$$p_d(r,\theta) = \frac{S_0\beta P_0^2\omega_d^2 e^{i\omega_d t}e^{-ik_d r}}{4\pi\rho_0 c_0^4 r}\left[\frac{1}{-2ik_d\sin^2(\theta/2)-2\alpha}\right] \tag{2.32}$$

Equation (2.32) can be simplified to:

$$= -\frac{S_0\beta P_0^2\omega_d^2 e^{i\omega_d t}e^{-ik_d r}}{8\pi\rho_0 c_0^4 r\alpha}\left[\frac{1}{1+\dfrac{k_d}{\alpha}\sin^2(\theta/2)}\right] \tag{2.33}$$

The expression in the brackets in Eq. (2.33) was first introduced by Westervelt. It is known as *Westervelt directivity function* in the literature (Westervelt, 1963). Equation (2.33) yields the amplitude of the difference wave in the far field. It has very narrow directivity and no side lobes as seen in Fig. 8. The -3 dB beam width of the difference wave is calculated as

$$2\theta_{1/2} = 4\sin^{-1}\left[(\alpha/k_d)^{\frac{1}{2}}\right] \tag{2.34}$$

Equation (2.33) can be written in the form of axial and directional pressure:

18

$$p(r,\theta) = P_{ax}(r)H(\theta)$$

$$P_{ax}(r) = -\frac{S_0 \beta P_0^2 \omega_d^2 e^{i\omega_d t} e^{-ik_d r}}{8\pi\rho_0 c_0^4 r\alpha} \qquad (2.35)$$

$$H(\theta) = \left[\frac{1}{1+\dfrac{k_d}{\alpha}\sin^2(\theta/2)}\right].$$
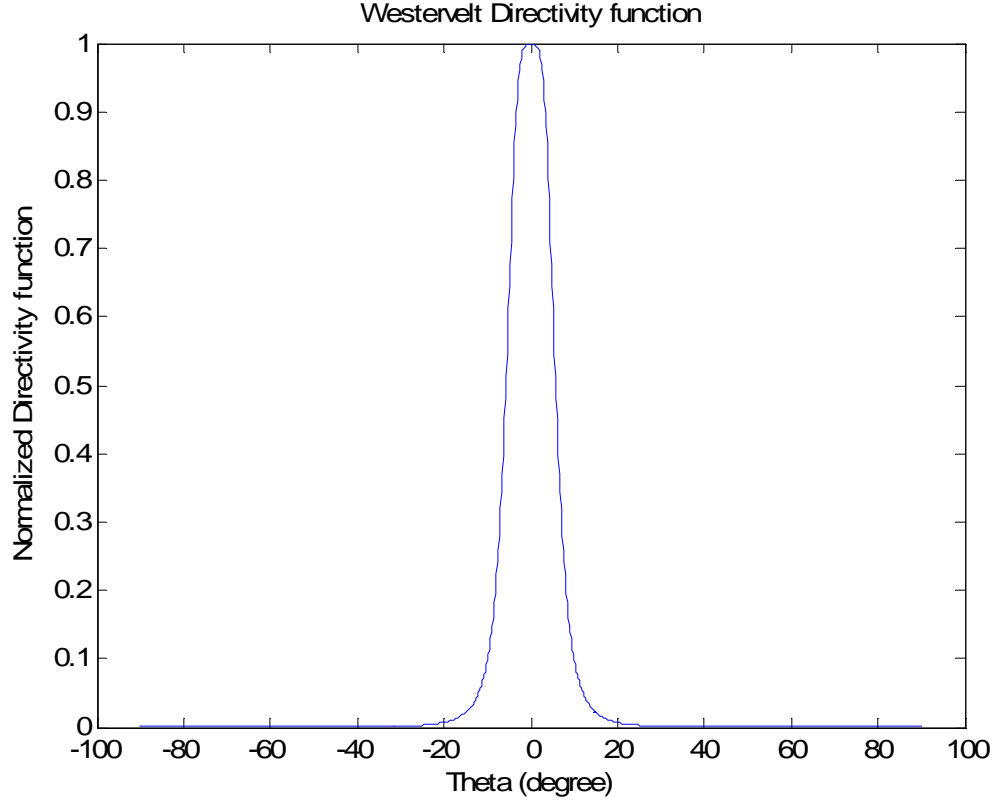
Figure 8.   Westervelt directivity function.

The important features displayed in Eq. (2.35) are that the far field the amplitude of the difference wave is proportional to *1/r*, inversely proportional to absorption coefficient of the primary waves, and proportional to square of the amplitude of both the primary wave and the square of the difference wave frequency.

Because the computation of the volume integral was done using the far field approximation, Eq. (2.35) does not show the linear growth of the difference frequency wave.

19

In order to see the difference wave generation in the near field, the perturbation method is applied to Eq. (2.15). First order and second order approximations were shown in Eq. (2.17) and (2.18). If Equation (2.14) is substituted into Eq. (2.18), ignoring the absorption of primary waves gives

$$\nabla^2 p_2 - \frac{1}{c_0^2}\frac{\partial^2 p_2}{\partial t^2} = \frac{\beta}{\rho_0 c_0^4}\frac{\partial^2 (P_0 \cos(\omega_1 t - k_1 x) + P_0 \cos(\omega_2 t - k_2 x))^2}{\partial t^2}. \qquad (2.36)$$

Squaring the sum of the two collinear beams in the right side of Eq. (2.36) will result in second harmonics, and sum and difference wave frequencies in the medium. Ignoring the second harmonics and the sum frequency wave, we end up with

$$\nabla^2 p_2 - \frac{1}{c_0^2}\frac{\partial^2 p_2}{\partial t^2} = \frac{\beta}{\rho_0 c_0^4}\frac{\partial^2 \left(2P_0^2 \cos(\omega_1 t - k_1 x)\cos(\omega_2 t - k_2 x)\right)}{\partial t^2}. \qquad (2.37)$$

Using the Fourier series decomposition, Equation (2.37) yields

$$p_2 = -\frac{\beta P_0^2 \omega_-}{2\rho_0 c_0^3} x\left[\sin(\omega_- t - k_- x)\right] \qquad (2.38)$$

Equation (2.38) shows that difference wave grows linearly with the distance up to a point where primary frequencies terminates due to the absorption. After this distance which is determined by Eq. (2.3), the difference wave will start to decrease proportional to *1/r* due to the spherical spreading.

2.   Berktay Approach

Westervelt assumed that the column of the primary waves is so narrow that the directivity of the aperture does not have any effect on the directivity of the difference wave. The assumption made by Westervelt was that the cross-sectional area of the primary waves is negligible compared to the square of the wavelength of the difference frequency wave. Westervelt also neglected the effects of the secondary wave absorption on the difference frequency amplitude. Berktay later included the directivity of the aperture as well as the absorption effects in his equation. The far field approximation of the Berktay's equation including absorption is then:

$$p(r,\theta) = \frac{P_1 P_2 \omega_-^2 S}{4\pi \rho_0 c_0^4 r} e^{-\alpha_- r} \frac{\cos(\omega_- t - k_- r - \beta)}{\left\{ A^2 + \left[2K\sin^2(\theta/2) \right]^2 \right\}^{1/2}} \tag{2.39}$$

where S is the surface of the aperture, and where

$$A = \alpha_1 + \alpha_2 - \alpha_- \cos(\theta)$$

$$\beta = \tan^{-1}\left(\frac{A}{2k_- \sin^2(\theta/2)} \right). \tag{2.40}$$

The directivity function of the aperture is added to Eq. (2.39), if the surface area of the aperture is large compared to λ^2 which is the wavelength of the difference wave. The directivity function of a circular aperture is given by the relation

$$\frac{2J_1(k_- a\sin(\theta))}{k_- a\sin(\theta)} \tag{2.41}$$

where a is the radius of the circular source. If the aperture is rectangular, the directivity function becomes

$$\frac{\sin(bk_- \sin(\theta))}{bk_- \sin(\theta)} \tag{2.42}$$

The geometry for this rectangular aperture in Berktay's calculations is shown in Fig. 9.
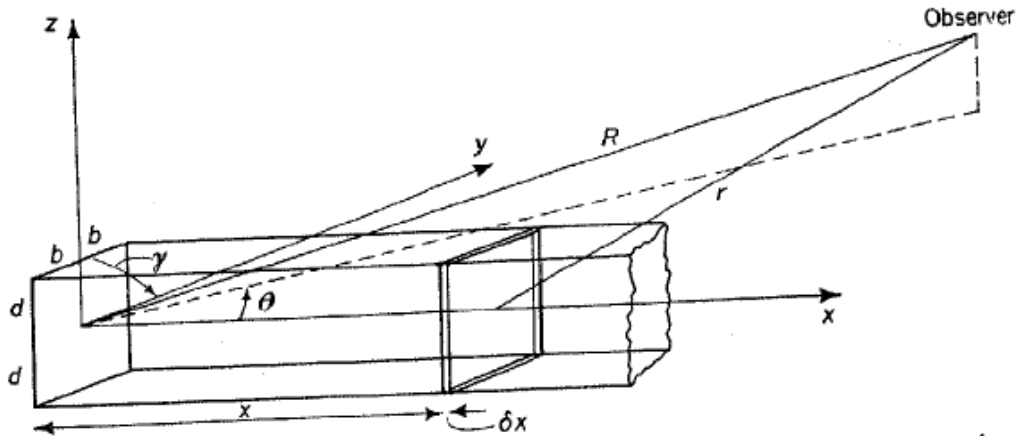
Figure 9.   The geometry used in Berktay's calculations, [From (Berktay, 1965)]

21

The 3 dB beam width of Berktay's equation can be calculated according to the Eq. (2.39) to be:

$$\theta_{1/2} = 2\sin^{-1}\left(\sqrt{\frac{A}{2k_-}}\right). \qquad (2.43)$$

The difference between the directivity function of the Berktay's equation and Westervelt equation is depicted in Fig.10.
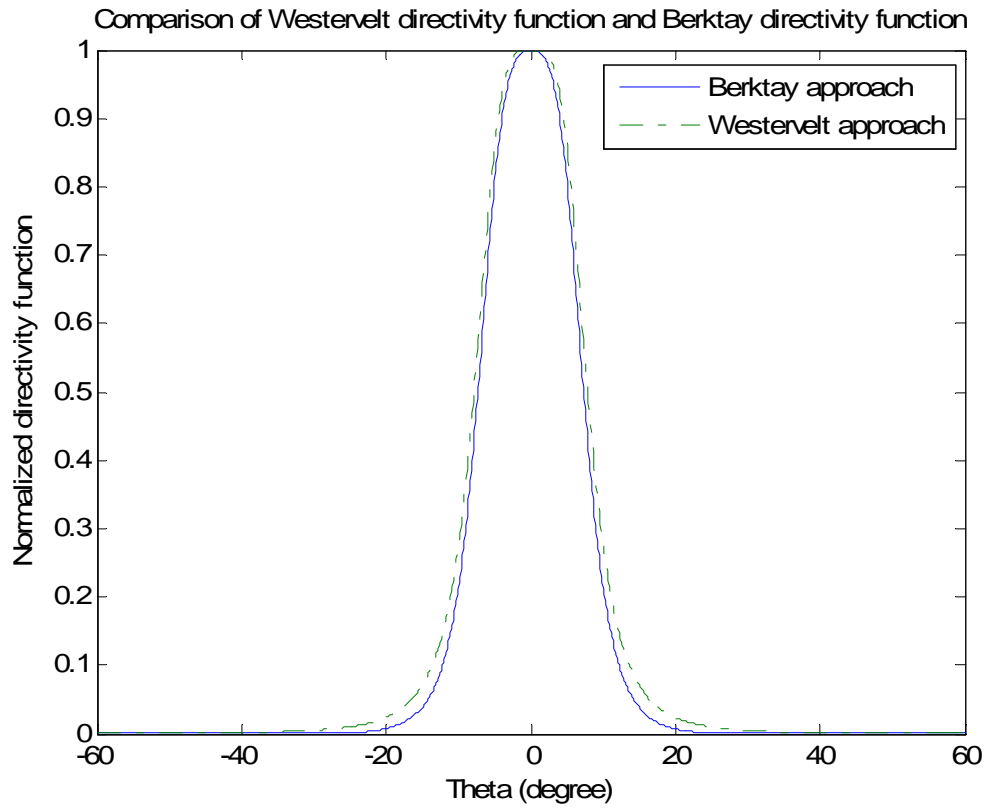
Figure 10.   Comparison of Westervelt's directivity function by Berktay's directivity function.

3.   Amplitude Modulation (Self-demodulation)

Another method for nonlinear generation of an audible frequency from ultrasonic frequencies is by amplitude modulation. In this case, the ultrasonic frequency is simply amplitude modulated by an audible frequency which then is demodulated in the medium through nonlinear effects. This process is also called *self-demodulation* because the

modulated audio signal is produced in the air by the nonlinearity effect. The beam pattern of the difference wave will also be as narrow as the main beam width and side-lobe free.

We consider the amplitude modulated wave

$$p_1(t) = P_1 E(t) \sin(\omega_c t - k_c x) e^{-\alpha x} \qquad (2.44)$$

where $E(t)$ is the modulation envelope, P_1 is the amplitude of the primary wave and ω_c is the ultrasonic carrier frequency. The modulation technique that is used in audio applications is generally a double side band amplitude modulation with the transmitted carrier (DSBAM-WC) (Mcclellan, Schafer & Yoder, 2003). The envelope function for this type of modulation is

$$E(t) = \left[1 + mg(t - \frac{x}{c_0}) \right] \qquad (2.45)$$

where $g(t)$ is the audio signal, and the m is the modulation depth.

The other amplitude modulation technique is double side band amplitude modulation with suppressed carrier (DSBAM-SC). It has the envelope function

$$E(t) = mg\left(t - \frac{x}{c_0} \right). \qquad (2.46)$$

In audio applications DSBAM-SC is not used because the generated difference wave is proportional to the square of the primary wave, as seen in the expressions below. Thus, the typical frequency spectrum of the audio signal $g(t)$ will be doubled in air.

By using Eq. (2.44) and (2.46) the source strength, q (Eq. (2.15)), can be calculated

$$q = \frac{\beta}{\rho_0^2 c_0^4} \frac{\partial}{\partial t} \left[P_1^2 \left(m^2 g^2(t - \frac{x}{c_0}) \right) e^{-2\alpha x} \sin^2(\omega_c t - k_c x) \right]. \qquad (2.47)$$

As seen from Eq. (2.47), squaring of the $g(t - x/c_0)$ will generate harmonics of the typical frequency spectrum of the function $g(t)$. Total harmonic distortion for this modulation is low compared to DSBAM-WC, because only the side bands are

23

interacting. There is no carrier frequency in the air. The frequency spectrum of the input signal for DSBAM-SC and DSBAM-WC is shown in Fig. 11.
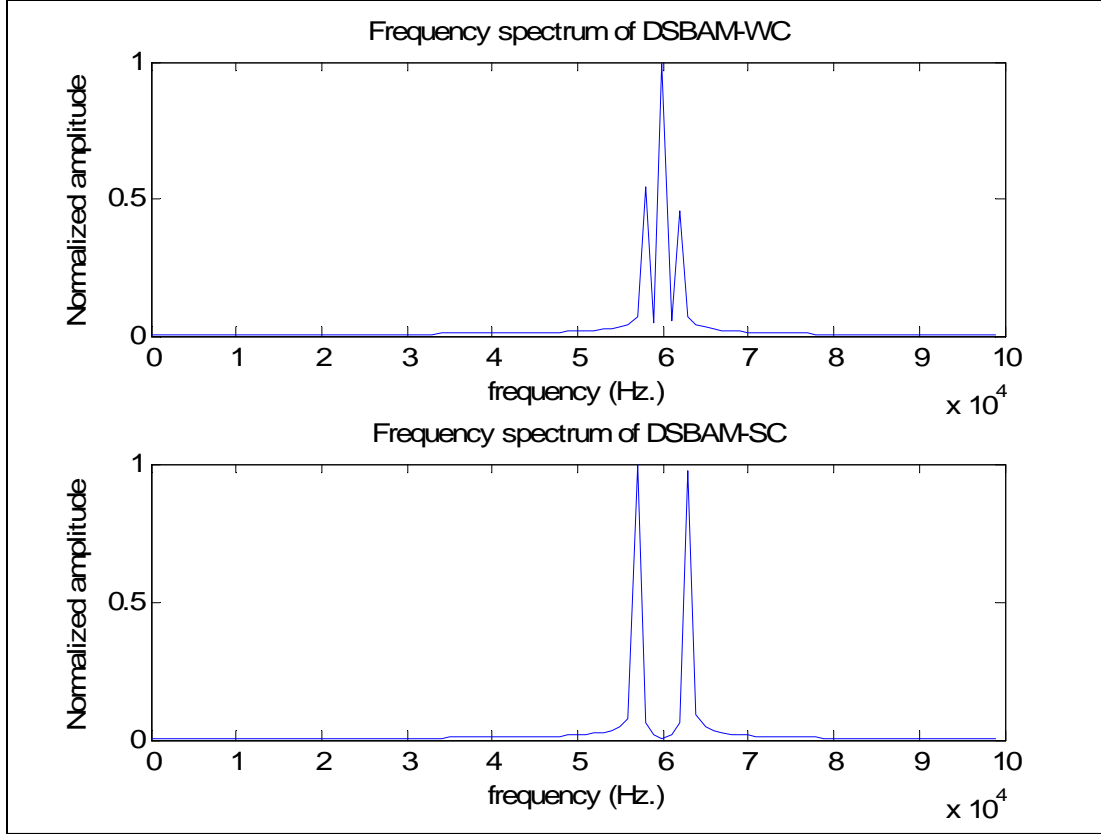
Figure 11. Frequency spectrum of the DSBAM-WC and DSBAM-SC. 60 kHz carrier frequency is amplitude modulated by 3 kHz signal.

If we use the DSBAM-WC as an input wave to the loudspeaker, the source strength becomes (Yoneyama et al., 1983)

$$q = \frac{\beta}{\rho_0^2 c_0^4} \frac{\partial}{\partial t} \left[P_1^2 \left(1 + 2mg(t - \frac{x}{c_0}) + m^2 g^2 (t - \frac{x}{c_0}) \right) e^{-2\alpha x} \sin^2(\omega_c t - k_c x) \right]. \quad (2.48)$$

The term $2mg(t - x/c_0)$ causes difference wave generation. Substituting Eq. (2.48) into Equation (2.22), yields the amplitude of the difference wave on axis

24

$$p_d(t,r) = \frac{\beta P_1^2 a^2 m}{8\rho_0 c_0^4 \alpha r} \frac{\partial^2}{\partial t^2} g\left(t - \frac{r}{c_0}\right). \tag{2.49}$$

The term $m^2 g^2(t - x/c_0)$ in Eq. (2.48) causes harmonic distortion. The harmonic distortion component may be represented as

$$p_h(t,r) = \frac{\beta P_1^2 a^2 m^2}{16\rho_0 c_0^4 \alpha r} \frac{\partial^2}{\partial t^2} g^2\left(t - \frac{r}{c_0}\right). \tag{2.50}$$

As seen in Eq. (2.49), the difference frequency is proportional to the second derivative of the function $g(t)$. Differentiation in the time domain brings $i\omega$ dependence in the frequency domain according to the Fourier transform property

$$\frac{d^k x(t)}{dt^k} \quad \square \quad (i\omega)^k X(i\omega) \tag{2.51}$$

Therefore, the second derivative operation will bring ω^2 dependence in the frequency domain. That means, the generated audio frequency has 12 dB/oct dependence. This feature requires using an equalizer before the amplitude modulation process (Yoneyama et al., 1983).

The harmonic distortion is proportional to m^2, therefore decreasing modulation depth will also decrease the distortion, while also resulting in lower sound pressure, because the generated audio signal is proportional to *2m*.

4.   Total Harmonic Distortion

In order to compensate for the effects of squaring and second derivative operation in Eq. (2.49) and (2.50), the audio signal should be preprocessed before it is being amplitude modulated. This technique was developed according to the Berktay's far field solution which gives the demodulated secondary wave that is proportional to the second time derivative of the modulation envelope. Therefore integrating twice and taking the square root before amplitude modulating will decrease the THD (Kite et al., 1998). The modulation envelope after preprocessing is

$$E'(t) = \sqrt{\left[1 + \int\int g(t)dt^2\right]} \; , \qquad\qquad (2.52)$$

which is illustrated in Fig.12.
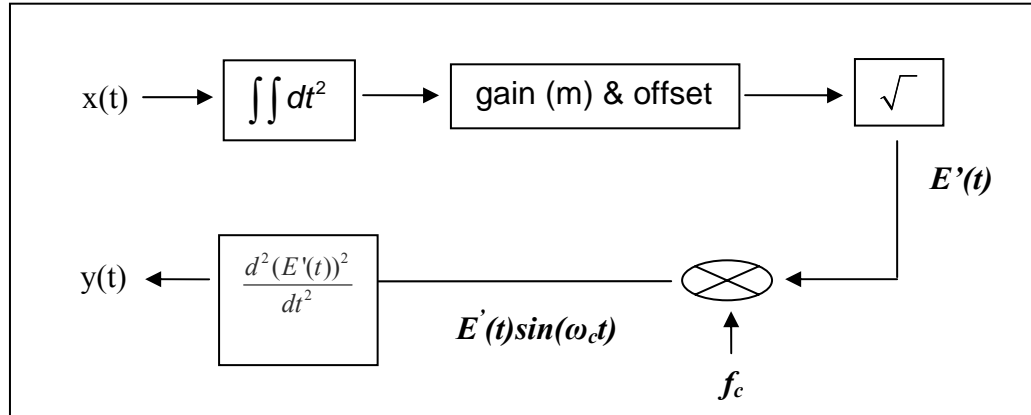
Figure 12.   Block diagram of preprocessing technique [After (Kite et al.)].

Preprocessing reduces the THD by about 5 percent, which may be still a problem for clean high fidelity audio production. One of the problems that is encountered in preprocessing technique is that the square root of the modulating envelope produces an infinite number of harmonics. The preprocessed envelope function for 60 kHz carrier will have a frequency spectrum as that shown in Fig. 13.
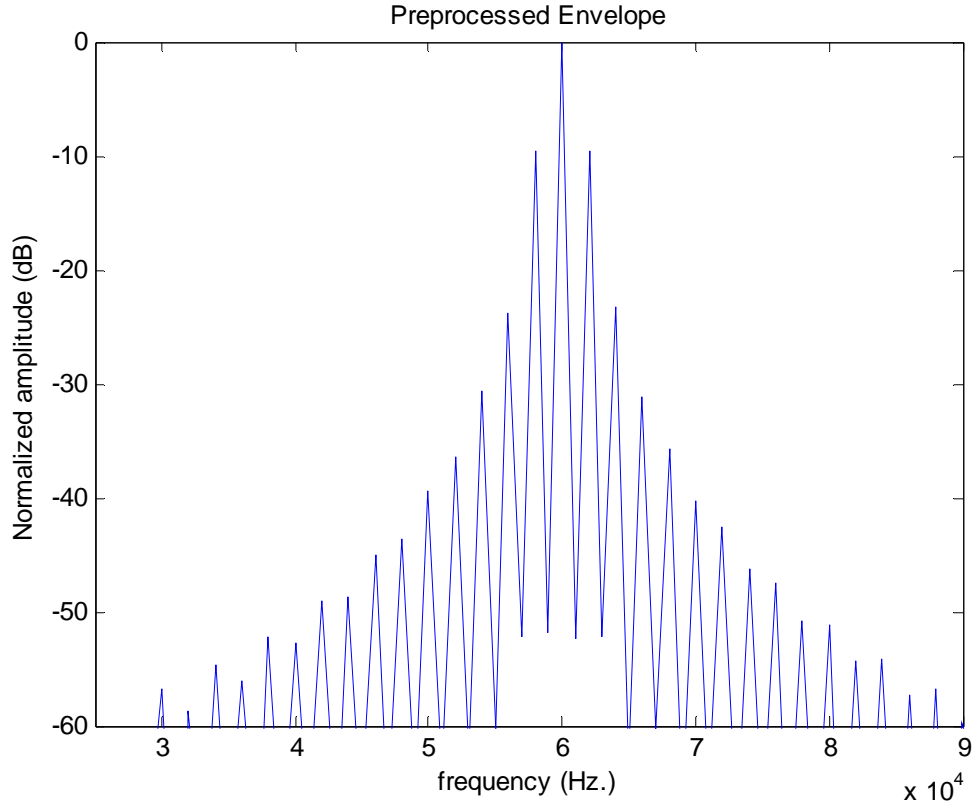
Figure 13.   Frequency Spectrum of the preprocessed envelope function.

The transducer must reproduce these harmonics in order to eliminate the distortion. Therefore, THD is also limited by the bandwidth of the transducer. A wideband ultrasonic sound source can reduce THD quite well so that it can be used as audio reproduction (Pompei, 1999).

D.   PARAMETRIC RECEIVERS

Nonlinear interaction of waves can also be applied for detecting a signal that comes from an arbitrary direction. This was also first suggested by Westervelt (1963). The theory that is used for investigating parametric receivers is the same as for parametric transmitters.

Parametric receivers consist of a pump wave, which emits an intense high frequency beam that is aligned with the receiver. The interaction occurs when the intense

high frequency pump wave is disturbed by an incoming weak low frequency wave. Illustration of parametric receiver is shown in Fig. 14.
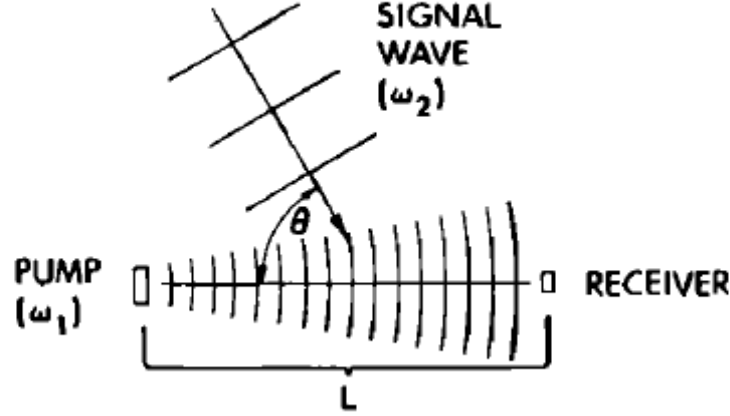
Figure 14.   Parametric receiver [From (Berktay & Muir, 1973)].

1.   Theory of Parametric Receivers

The features of the parametric receivers are very similar to those of linear continuous end-fired arrays but parametric receivers have only two elements. One of them is the pump source and the other one is the receiver. Therefore, the distance between them is an important parameter that should be taken into account.

One of the biggest differences between parametric transmitters and receivers is that the interaction takes place between an intense high frequency spherical wave and a weak low frequency plane wave. The analytical model for the generated difference sound wave is the same as the one for parametric transmitters. The resultant sound wave is given by (Barnard, Willette, Truchard & Shooter, 1972)

$$p_d(R_0,t) = \frac{-\rho_0}{4\pi} \int \frac{\partial q}{\partial t} \left\{ \frac{e^{\left(i(k_d+i\alpha_d)|R_0-r|\right)}}{|R_0-r|} \right\} dV. \tag{2.53}$$

Volumetric integration of Eq. (2.53) gives the amplitude of the sum and difference frequency at a distance L from the pump transducer:

$$p_{\pm} = \frac{(\omega_1 \pm \omega_2)\beta P_1 P_2}{2\rho_0 c_0^{\ 3}} e^{\left[-(\alpha_{\pm} + jk_{\pm})L \pm jM\right]} D(\theta)$$

$$D(\theta) = \frac{Sin(M)}{M} \quad \text{and} \quad M = \frac{1}{2}k_2 L(1 - \cos(\theta))$$

(2.54)

where ω_1 is the pump frequency, ω_2 is the low frequency incoming wave and L is the distance between the pump transducer and receiver. As can be seen from Eq. (2.54), the directivity pattern of the sum or difference wave is only dependent on the distance between pump and receiver and the frequency of the incoming low frequency wave. The directivity of the sum and difference wave is the same, and the directivity of the pump source does not affect the directivity of the sum and difference wave. The 3 dB beam width of the secondary wave is given by

$$\theta_{1/2} = 4\sin^{-1}\left(0.47\left(\frac{\lambda_2}{L}\right)^{1/2}\right).$$

(2.55)

2. Parametric Receiver Arrays

The parametric receiver has a beam width that is inversely proportional to the square root of the characteristic length, shown in Eq. (2.55), while the beam width for conventional array is inversely proportional to its length. Therefore, it is very difficult to increase the resolution without requiring very long distances between pump and receiver. If we consider building arrays of parametric receivers, both the beam width of the secondary wave will decrease and the minor lobes will be more suppressed, furthermore the array configuration makes the parametric receiver possible to be steered to a desired angle (Berktay & Muir, 1973). Illustration for parametric receiver array is seen in Fig.15.
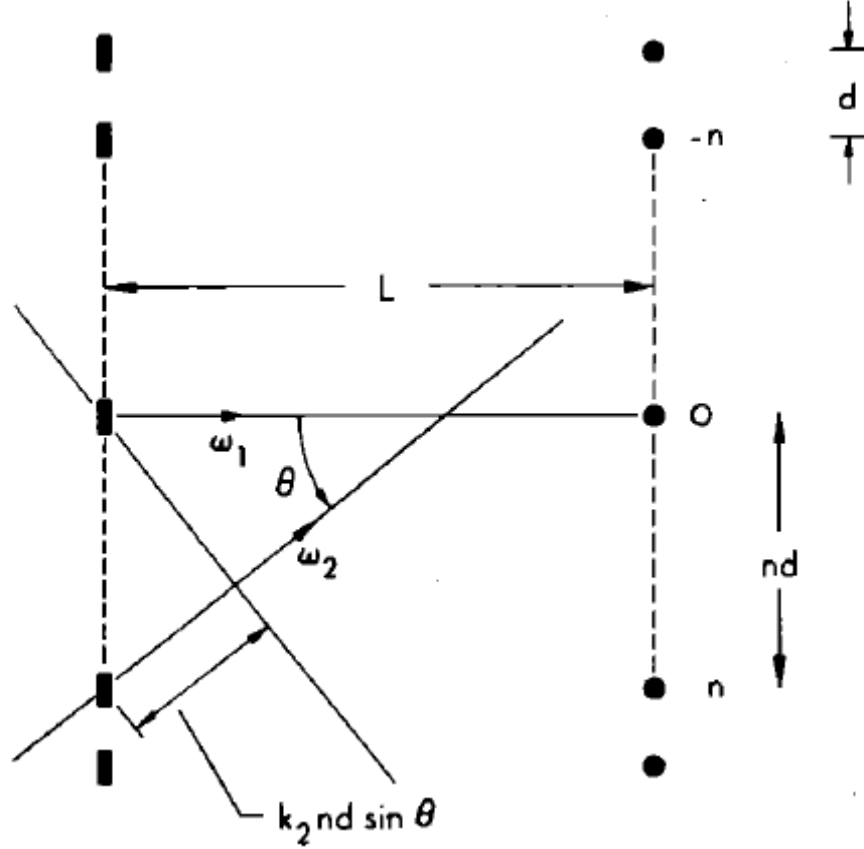
Figure 15.   Parametric receiver array [From (Berktay & Muir, 1973)].

If the directivity function of the each element is defined as $D(\theta)$, directivity function of the array becomes

$$D_t(\theta) = D(\theta)D_b(\theta)$$
(2.56)

where $D_b(\theta)$ is the directivity function of the array when omni-directional point sources are used. The total directivity function of the parametric receiver array can be found if the outputs add in phase:

$$D_t(\theta) = \cos\left(\frac{k_2 d \sin(\theta)}{2}\right)\frac{\sin\left(\frac{1}{2}k_2 L(1-\cos\theta)\right)}{\frac{1}{2}k_2 L(1-\cos\theta)}$$
(2.57)

where d is the distance between parametric receivers.

30

III. MODELING OF PARAMETRIC ARRAYS BY LINEAR END-FIRED ARRAYS

When compared to conventional piston sources, parametric end-fired arrays are more directional and have a nearly sidelobe-free beam pattern at low frequencies. The mechanism that makes the parametric arrays so unique is the nonlinear interaction of the ultrasonic frequencies in the confined volume. In order to develop a better understanding of the parametric arrays, we need to look more closely at the theory of linear line arrays. In this chapter we will develop the theory of linear end-fired line arrays and compare it to conventional piston sources.

A. LINEAR LINE ARRAY BASICS

For linear arrays, the -3 dB half power point is determined by (Kinsler et al., 2000)

$$\sin\theta = \frac{\lambda}{l} \tag{3.1}$$

where λ is the wavelength, and l is the length of the array. A longer array yields a more directional the beam pattern in the far field of the aperture. However, it is not always desirable to increase the length of the array because of the practical and operational concerns. Highly directional beams can also be generated by increasing the frequency. This also has a drawback because high frequencies suffer from absorption more than low frequencies. Figures 16 and 17 show that increasing both the length and the frequency of the array results in a narrower main beam.

Shown also in Figure 16 and 17 are sidelobes, which are a major issue that should be taken into account. There are some methods to decrease the side lobes to a reasonable degree. Applying an amplitude window to the elements of the array suppresses the side lobes, which meanwhile, widens the main lobe. Figure 18 depicts the beam pattern of the line array, when a Hanning window is applied. Amplitude of each simple acoustic source is multiplied by a weighting that is determined by

$$\omega(k) = 0.5 \times \left(1 - \cos\left(2\pi \frac{k}{n+1}\right)\right), \qquad k=1,...,n \qquad (3.2)$$

where n is the total number of simple acoustic source in the line array.

Theoretical plots seen in Figure 16, 17 and 18 are plotted in the far field region of the line array. Simple discrete sources make up the line array which can also be thought as a continuous line source when the spacing between simple sources is so small. Beam pattern of the line array (Figure 16-17) in the far field (Fraunhofer region) is given by

$$H(\theta) = \left| \frac{1}{N} \frac{\sin\left[(N/2)kd\sin\theta\right]}{\left[(1/2)kd\sin\theta\right]} \right| \qquad (3.3)$$

where N is the number of simple acoustic sources, k is the wave number, d is the spacing between the sources and θ is the angle from the acoustic axis of the source.
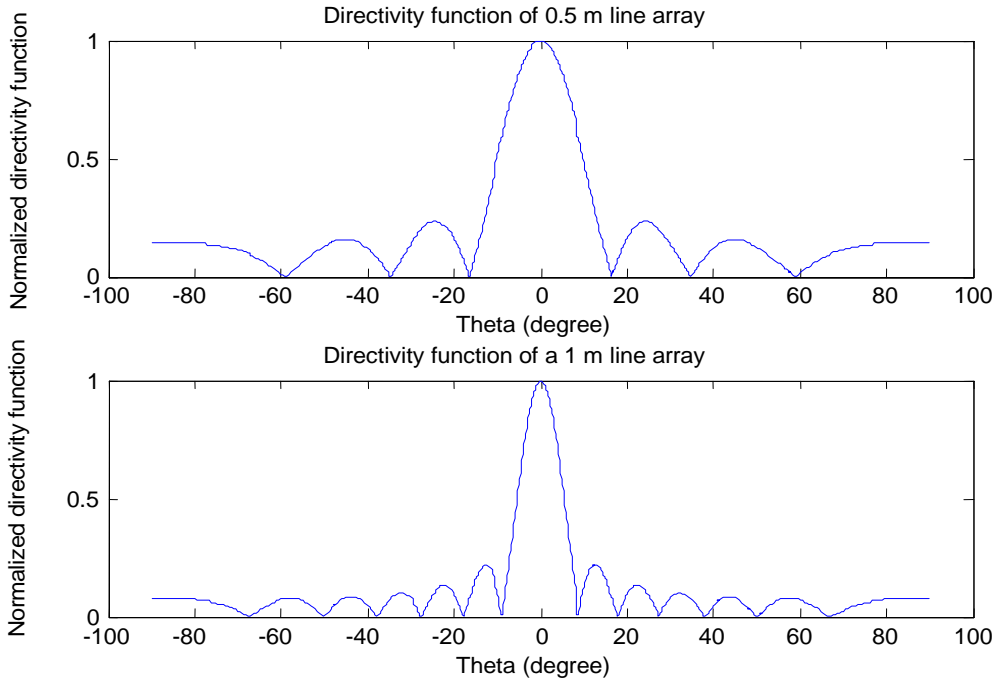
Figure 16.   The far field beam pattern of the line array of frequency 2 kHz. The longer array has narrower main beam. The length of the array for the first plot is 0.5 m. The length of array for the second plot is 1 m.
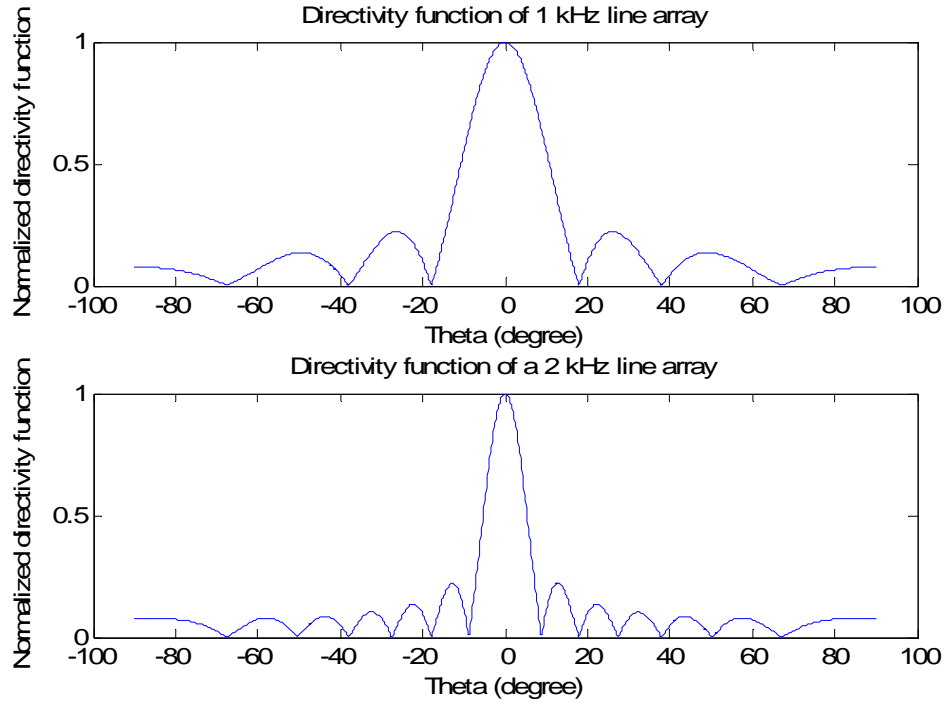
Figure 17.   The far field beam pattern of the array. The higher frequencies yield narrower main beam patterns.
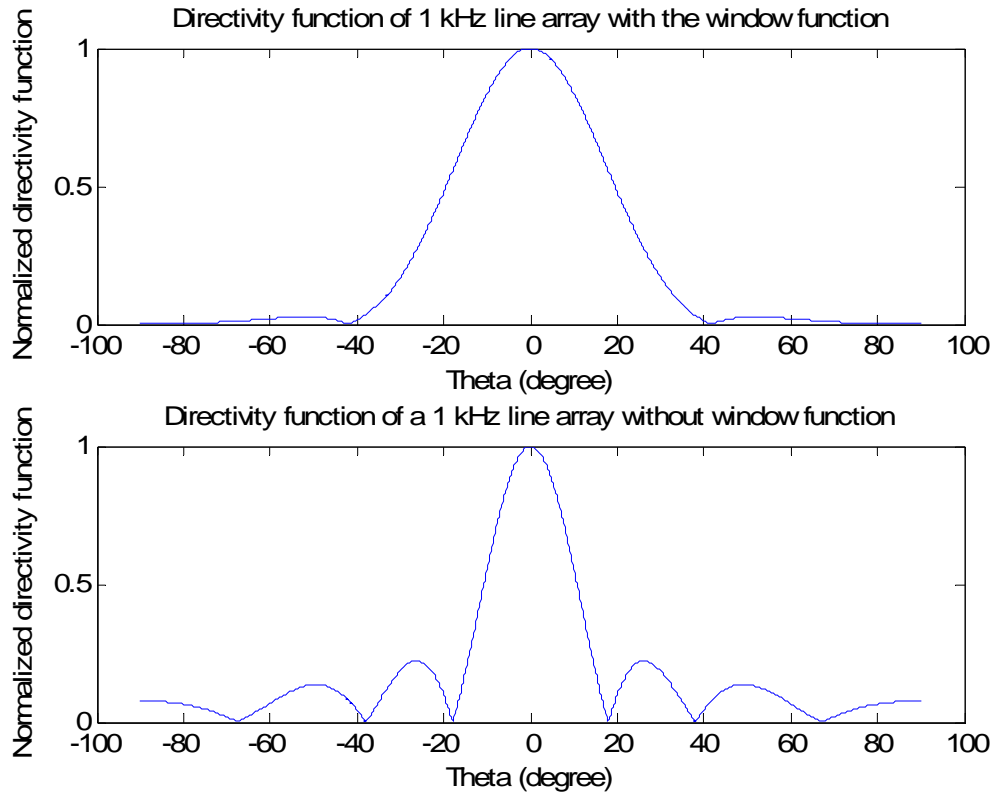
Figure 18.   The far field beam pattern of the line array. Top figure is the result of using a Hanning window. This has reduced the side lobes at the expense of wider beam width.

The main lobe of acoustic arrays can be steered to any direction by applying phase differences between the array elements. It is called *end-fired* array when the maximum radiation from the source is along the axis of the array. For an end-fired array configuration, the phase difference between the elements should be π when the spacing between elements is a half wavelength. Beam pattern of a steered line array is given by

$$H(\theta) = \left| \frac{1}{N} \frac{\sin\left[(N/2) kd \left(\sin\theta - \sin\theta_0 \right) \right]}{\left[(1/2) kd \left(\sin\theta - \sin\theta_0 \right) \right]} \right| \tag{3.4}$$

As seen in Fig. 19, steering the major lobe to end–fire results in widening the major lobe.

B.   MODELING PARAMETERS

The idea of modeling a parametric end-fired array with a linear end-fired array comes from the fact that the nonlinear interaction of the ultrasonic primary signals can be thought as made up of a virtual array in the medium that generates the secondary wave, which is terminated by the natural absorption in the medium. These virtual point sources extend continuously along the interaction length. Therefore the length of the linear end-fired array in our model will be determined by the absorption of the primary signal. Since the length of the array is one of the main factors that determine the narrowness of the beam pattern, the longer the array length, the narrower the main beam. High absorption coefficients make the interaction length shorter causing wider major lobe. The interaction length is calculated from Eq. (2.3):

$$L = \frac{1}{2\alpha},$$

where α is the absorption coefficient in Neper/meter for the mean frequency of the two primary signals.
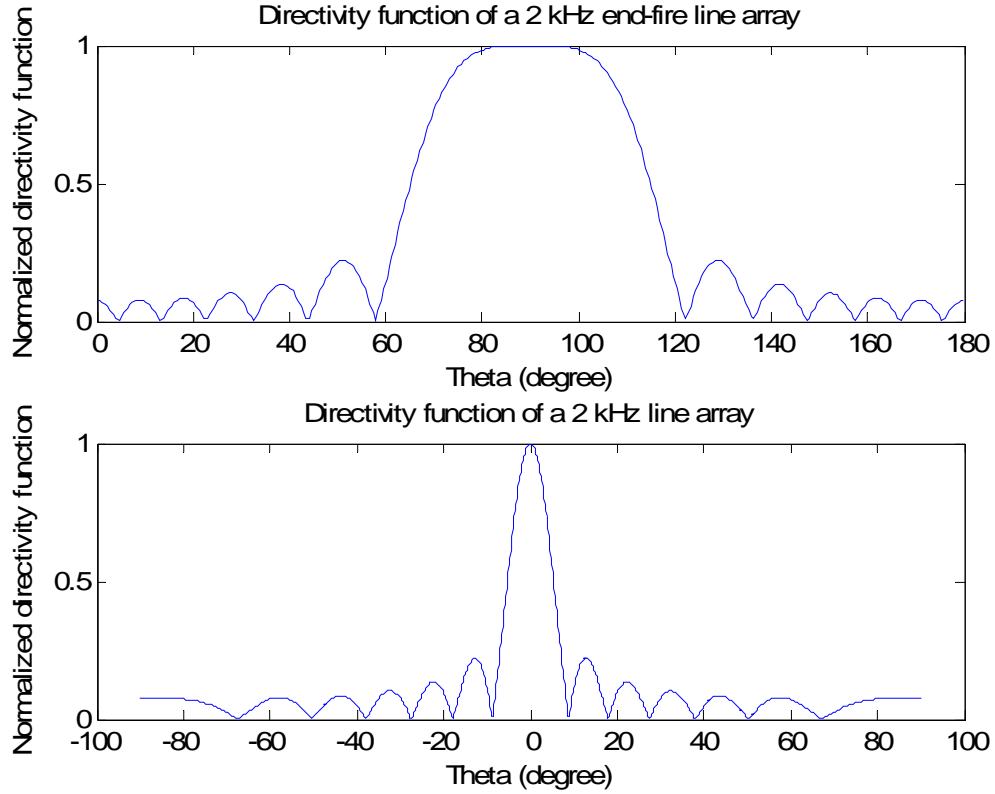
Figure 19.   Comparison of the far field beam pattern of a 2 kHz, 2 m long end-fired line array (top) and broadside line array (bottom). The end-fired array steering results in a wider main lobe.

The side lobe free beam pattern of the parametric arrays result from an exponential tapering of the primary signals due to the absorption. Therefore, exponential tapering will be applied to the array elements in our model.

The maximum spacing between the array elements is adjusted as *λ/2* to prevent grating lobe formation in the model. Since we are assuming that the virtual point sources extend continuously along the interaction length, one is tempted to have as small spacing as possible between the array elements. As it will be seen, the spacing between elements does not significantly affect the beam pattern of the difference signal.

The absorption of sound in air is caused by two mechanisms. One mechanism is due to transport effects such as viscosity, thermal conduction, and internal friction. The other mechanism is molecular thermal relaxation, which is related with the internal structure of the molecules and interaction between them (Bass, Bauer & Evans, 1972).

Water vapor in air contributes to the absorption in air due to the collision with nitrogen and oxygen molecules. Therefore, humidity of the air plays an important role. It is insufficient to use the classical absorption coefficient in our applications. Figure 20 is a plot of the absorption coefficient in air which incorporates both the classical absorption coefficient and absorption due to the effects of humidity. For example, at 20˚C, 1 atm and 50% relative humidity, the absorption coefficient of a 60 kHz sound wave in air is found from the graph in Fig. 20 to be 1.5 dB/m, which is equal to 0.1724 Neper/m.
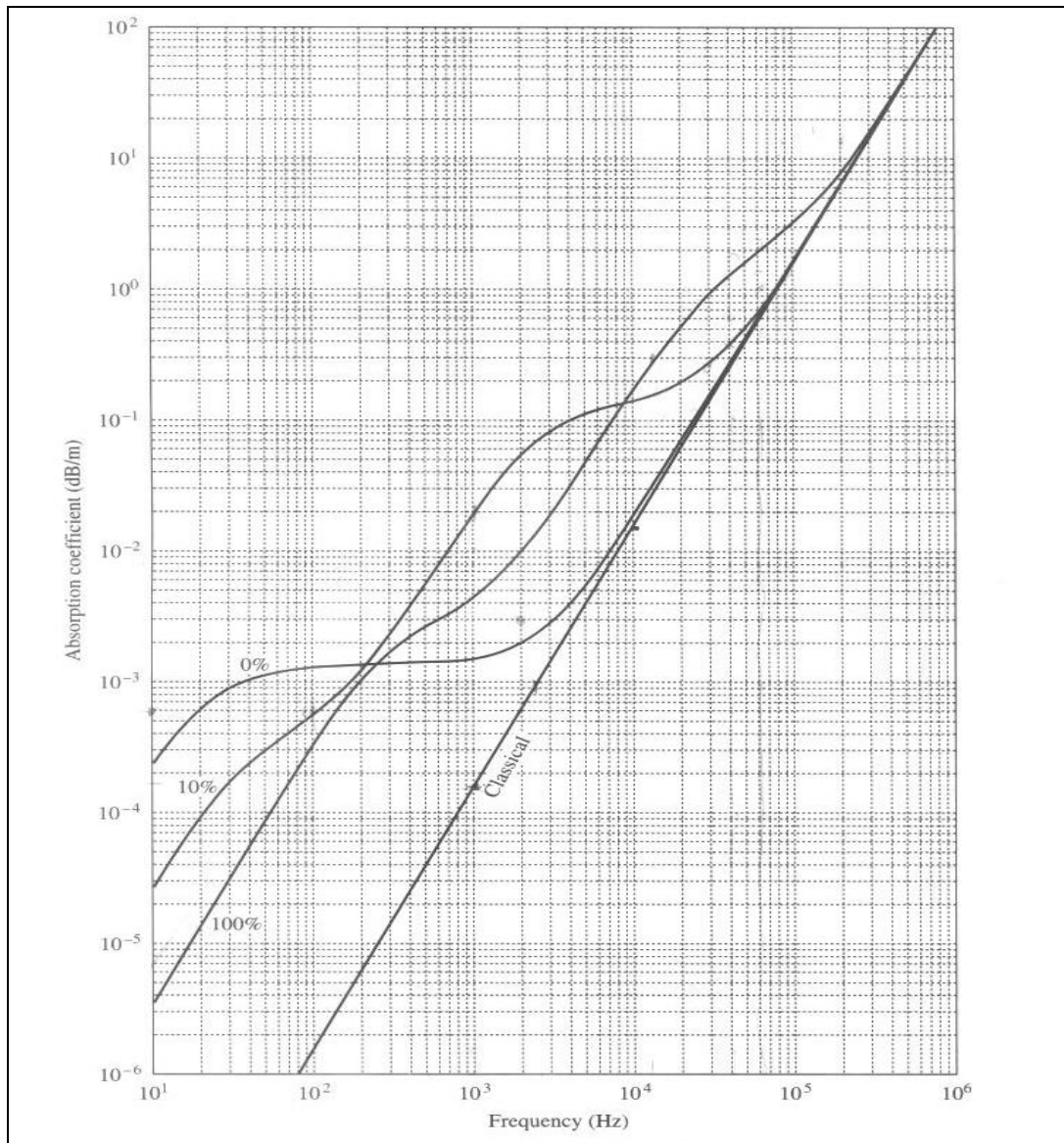

Figure 20.   Absorption of sound in air at 20°C and 1 atm for various relative humidities.
[From (Kinsler et al., 2000)]

C.   CONSTRUCTION OF THE MODEL AND COMPARISON WITH THEORY

In our model, the linear array consists of point sources that emit a 2 kHz signal. The sources are separated by $\lambda/2$ from each other. The length of the array is determined from the absorption of ultrasonic frequencies, because it should be equal to the nonlinear interaction length of the parametric array. From Equation (2.3), the interaction length for a 60 kHz ultrasonic wave is calculated to be 2.9 m which will be our array length. The wavelength of sound can be determined from,

$$\lambda = \frac{c}{f} \tag{3.5}$$

where c is speed of sound (343 m/s in air) and f is the frequency of interest in Hz. For a 60 kHz signal, the wavelength is 0.57 cm, thus yielding a spacing between elements of 0.29 cm which is much smaller than the wavelength of the 2 kHz signal of interest. Along the interaction length, there are 35 elements, exponentially tapered from the beginning of the array due to absorption of ultrasonic signal.

D.   SIMULATION RESULTS

Since the beam pattern of the parametric end-fired array highly depends on the interaction length, we have developed two models have been corresponding to two different array lengths. In the first model, the interaction length is set as

$$L = \frac{1}{2\alpha}$$

in accordance with Pompei's work (1999). Figure 21 shows the untapered and exponentially tapered end-fired array as being nearly the same. The interaction length for this situation is 2.9 m, which is not sufficient for suppressing the side lobes.

If we compare the tapered end-fired array model with the conventional baffled piston source with radius 0.22 m (same with the Audio spotlight) operating at 2 kHz, the conventional piston source has higher side lobes compared to the model (Figure 22) but the directivities of both are almost same. The comparison between the model and the Westervelt directivity function is shown in Fig. 23. Thus we can conclude that the

current model is not close to the theory both in directivity and in side lobe pattern mainly because the array length is too short.
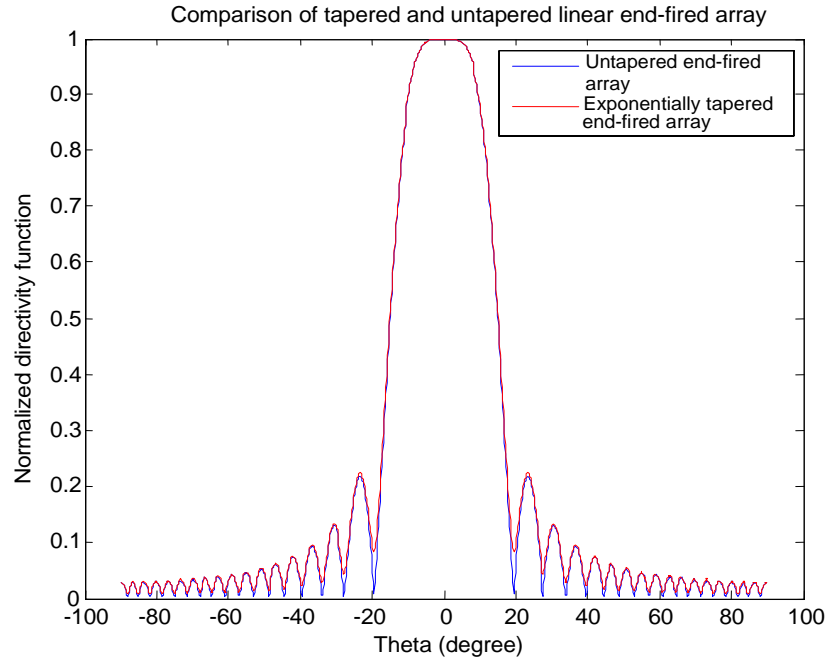
Figure 21.   The far field directivity function of untapered and exponentially tapered 2 kHz end-fired array. The blue line represents the untapered array while the red line is the tapered end-fired array.

Figure 22.   The far field directivity function of the conventional baffled piston source and exponentially tapered linear end-fired array.

Figure 23.   The far field directivity function of tapered linear end-fired array (solid curve)
compared with Westervelt theory (dashed curve).

We now consider an interaction length eight times longer,

$$L = \frac{4}{\alpha}$$

which corresponds to an array 23.2 m long with 272 point sources. Compared to conventional piston source that has radius 0.22 m, Fig. 24 shows the exponentially tapered linear end-fired array with suppressed sidelobes and a narrower main beam. Furthermore, the beam directivity now resembles Westervelt's directivity function, as shown in Fig. 25.
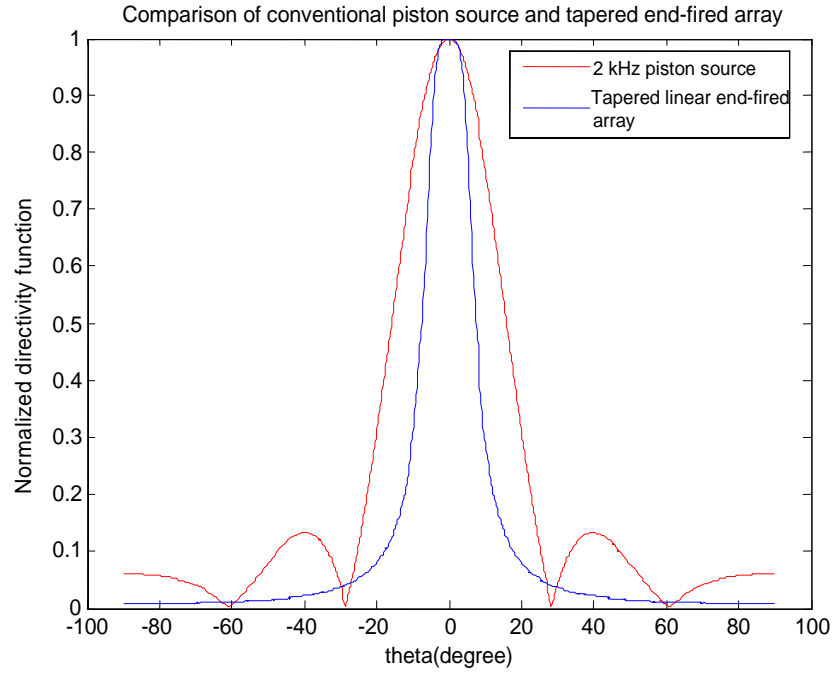
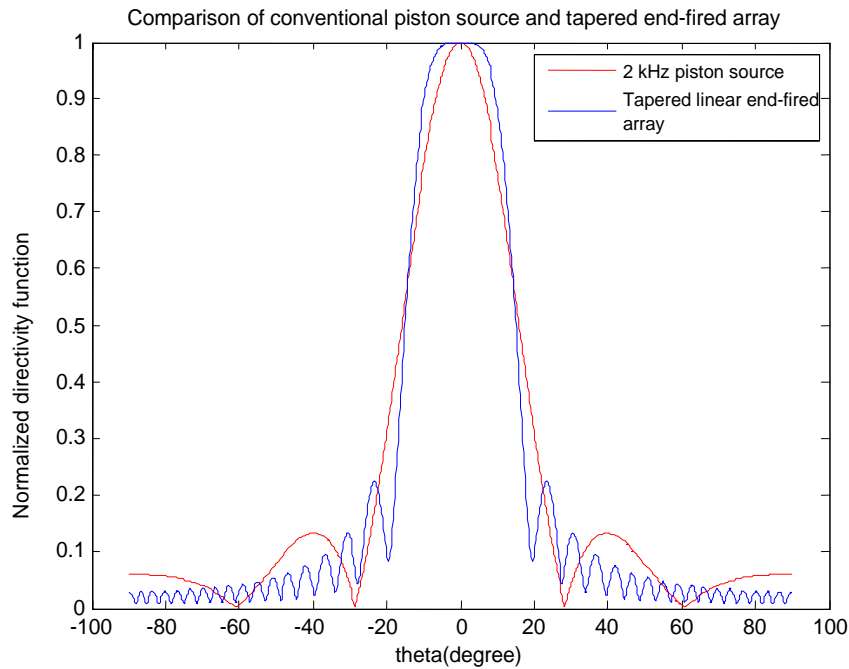Figure 24.   The far field directivity function of the conventional baffled piston source (dashed curve) and the exponentially tapered linear end-fired array (solid curve).
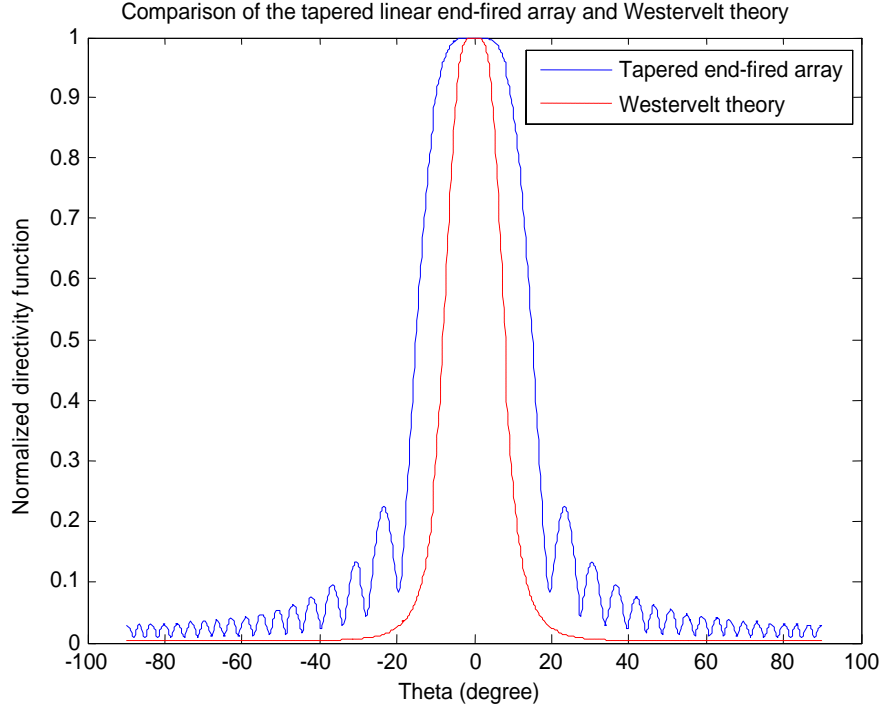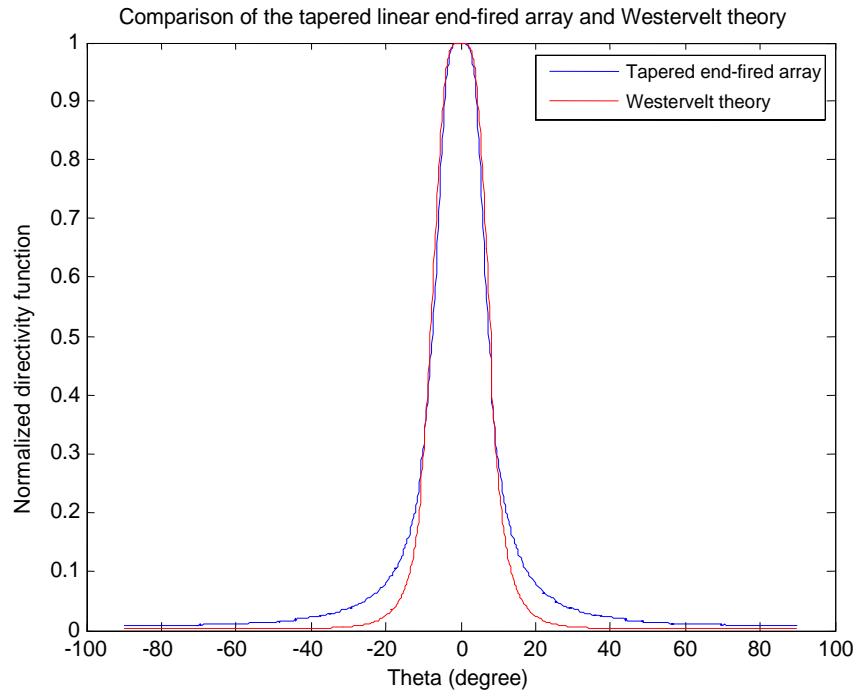

Figure 25.   The far field directivity function of tapered linear end-fired array and Westervelt theory.

The radius of the source determines the directivity of conventional baffled piston sources. The bigger the source, the narrower a beam pattern can be achieved. In our calculations we found that in order to get the similar beam pattern with the tapered linear end-fired array, a piston source with a 0.55 m. radius is needed. Figure 26 shows the comparison between the piston source and linear tapered end-fired array.
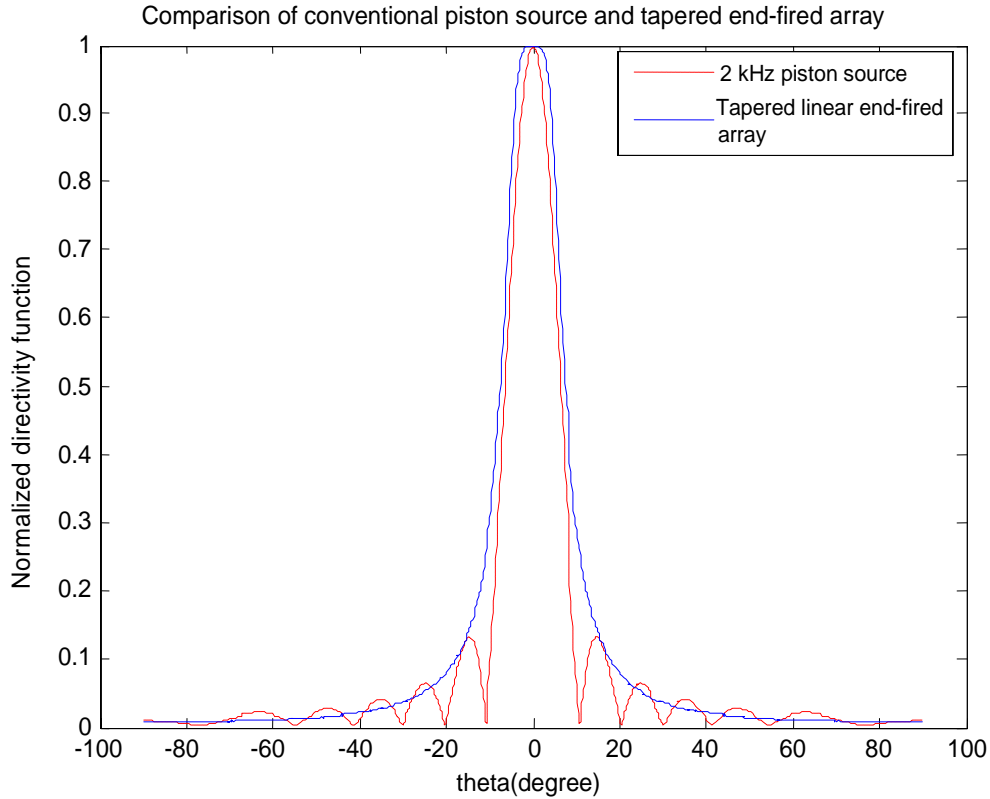
Figure 26.   The far field directivity function of the 0.55 m. radius piston source and linear tapered end-fired array.

THIS PAGE INTENTIONALLY LEFT BLANK

IV.   COMPARISON OF EXPERIMENTAL RESULTS WITH THEORY

In this chapter, experimental results are presented. A controlled parametric output from a Holosonic™ loudspeaker was been used in the experiment to examine, investigate and compare the theoretical results with the experimental data. The theoretical results are based on Westervelt theory, which is explained thoroughly in Chapter II of this thesis.

In order to eliminate the interference due to reflections from boundaries and minimize the ambient noise, we conducted the experiment in an anechoic chamber, located in the basement of Spanagel Hall at NPS (Figure 27). The anechoic chamber has usable dimensions of 8.23 m × 4.26 m × 3.35 m. For frequencies above 100 Hz, it is capable of absorbing 99% of the sound energy that reaches the boundaries.

The experimental set-up shown in Figure 27 consists of the parametric loudspeaker, which is driven by an HP 8904A multifunction synthesizer. The HP 8904A has the capability of generating two different frequency signal waveforms, referenced to a common time base and absolute amplitude. Furthermore, it can also amplitude modulate any signal which, as we will see, is required for total harmonic distortion measurements.

Two different kinds of microphone were used in the measurements due to their sensitivities in different frequency bands. The B&K 4136 (1/4'' free field) was used for the primary frequency signal measurements due to its wide band frequency spectrum (20 Hz-80 kHz) which covers the 60 kHz resonant frequency of the parametric array. The difference frequency signal was captured by a G.R.A.S. 40AF (1/2" free field) microphone, which has a frequency band between 3.15 Hz and 20 kHz and a higher sensitivity (1.15 mV/Pa) than the B&K 4136. An SR-560 low noise pre amplifier provided low-noise amplification when the signal level from the microphone is weak. The SR-560 also contains two first–order R-C filter which are used for eliminating frequencies below 300 Hz and above 100 kHz. The frequency spectrum and time domain of the output signals are measured by an SR 785 dynamic signal analyzer and a Tektronik TDS 3054B oscilloscope respectively. In order to measure the beam pattern for the

difference frequency, an measurements, the frequencies other than difference frequency SR-650 high pass/low pass elliptical filter was used, which consists of an 8-pole 6-zero elliptic-type filter with an 115 dB per octave roll-off.

Figure 27.   Parametric end-fired array in NPS anechoic room.

Figure 28 shows a picture of the equipment rack fitted with the instrumentation to perform both types (range and beam pattern) of measurements.
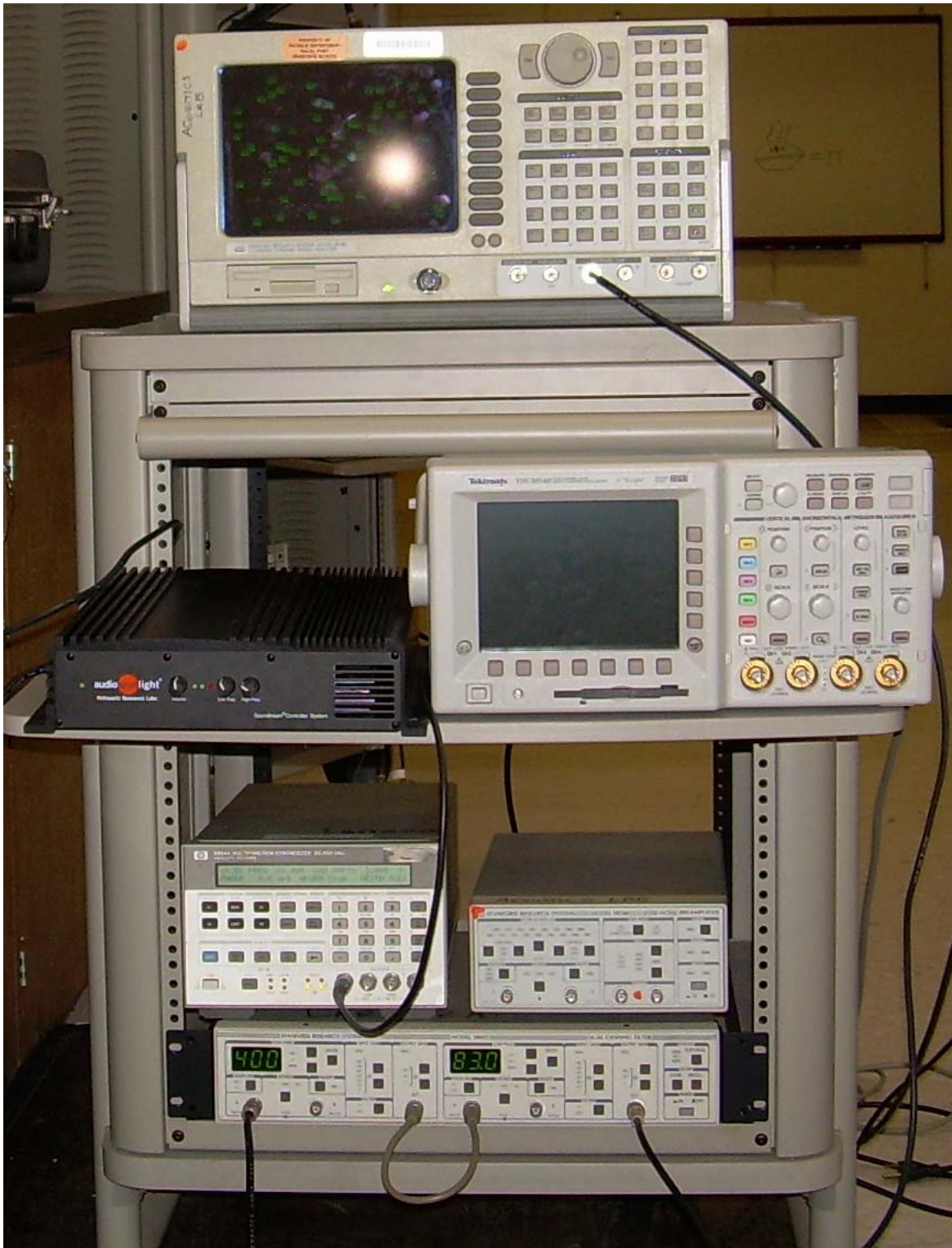
Figure 28.   Instruments used in the experiment.

A.   BEAM PATTERN OF THE DIFFERENCE WAVE

Due to absorption, both the sum frequency and primary frequency signals decay faster than the difference frequency signal. Thus, at long distances the beam pattern contains only the difference signal. In addition, ultrasonic frequency signals are beyond the audible range. In order to measure the characteristics of the difference frequency beam pattern, both the primary and sum frequency signals are filtered out in the experimental set-up shown in Fig.29
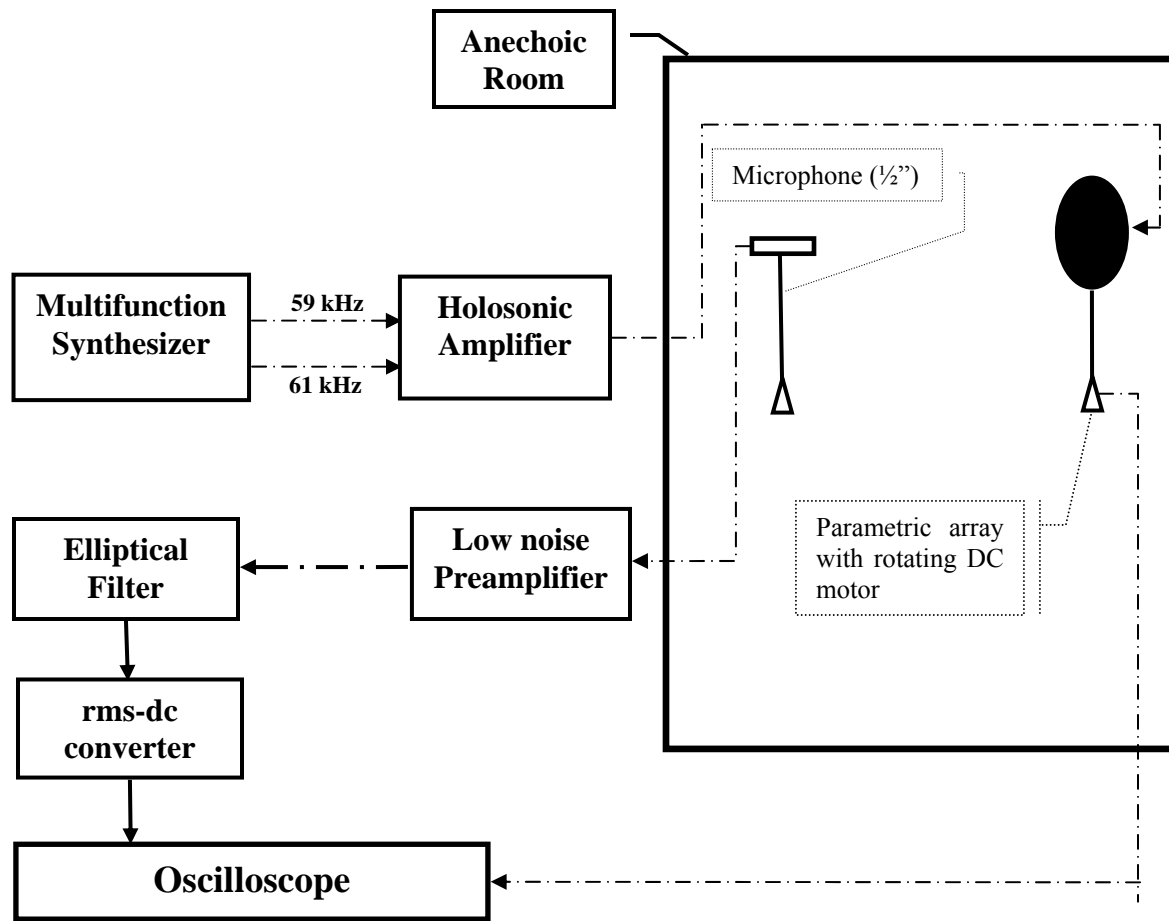
Figure 29.   Experimental set-up for beam pattern measurements of the parametric array.

In this arrangement, the microphone was placed at 5.36 m from the parametric array and aligned with its acoustic axis. The HP 8904A multifunction synthesizer

generated two 2 V peak sinusoidal signals with frequencies 59 kHz and 61 kHz. These ultrasonic signals comprise the primary waves input to the parametric array. Due to the nonlinear interaction of the ultrasonic waves in the medium, a 2 kHz sinusoidal difference signal is produced in the air. Using a ½" G.R.A.S 40AF microphone, the pre-amplified signal was filtered by the SR-650 elliptical filter with a band pass filter around 2 kHz, which filtered out harmonics of the 2 kHz signal, the primary signals, and the sum frequency signal. This filtered output was then used as the input into an RMS-DC converter, where the RMS values of the 2 kHz signal can be recorded for one full rotation of the parametric array in order to determine the beam pattern of the parametric array in the oscilloscope, referenced to the control box of the DC motor, which rotates the parametric array. As shown in Figures 30 and 31, the beam pattern has almost no side lobes and a very narrow main beam as determined by *Westervelt directivity function*.
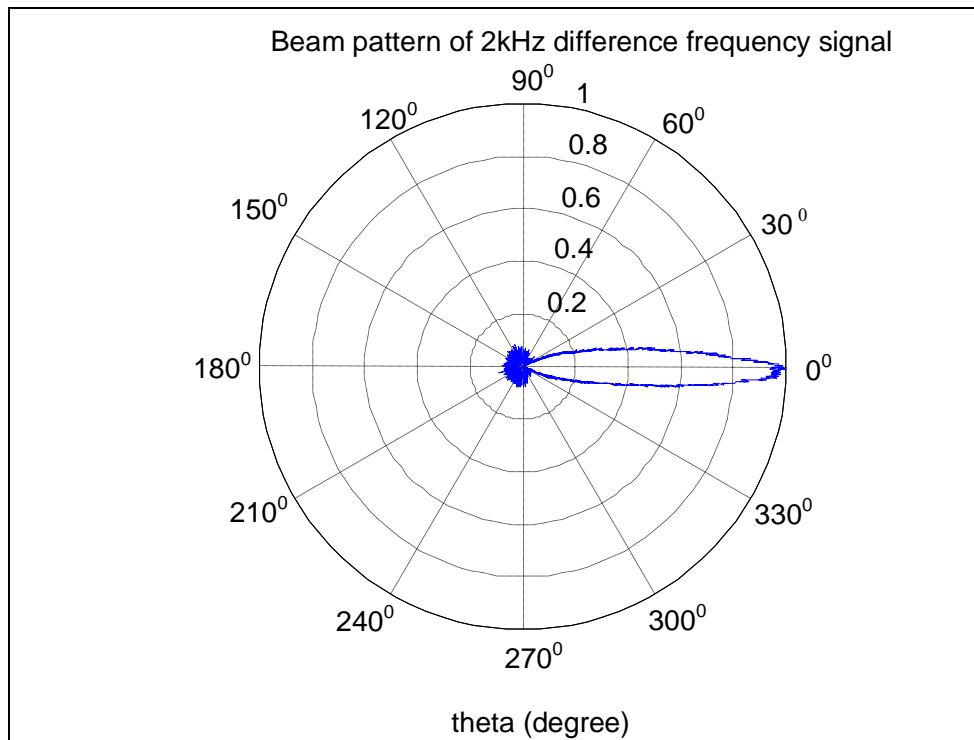
Figure 30.   Beam Pattern of the 2 kHz difference frequency signal.
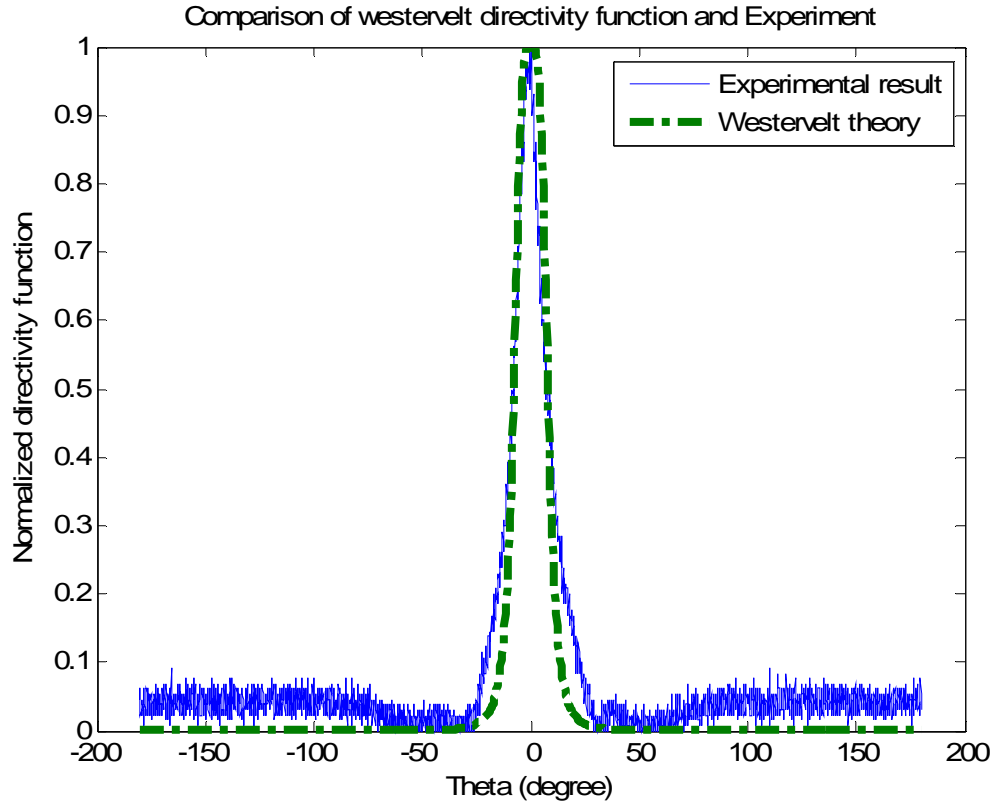
Figure 31.   Comparison of the beam patterns of the experimental data for 2 kHz signal and Westervelt directivity function.

A conventional piston source with the same radius as the parametric array would give the beam pattern shown in Fig. 32 for a 2 kHz operating frequency. The advantage of the parametric array is apparent from this figure since a conventional piston source with the same operating frequency and radius would have wider beam width and a higher side lobe.
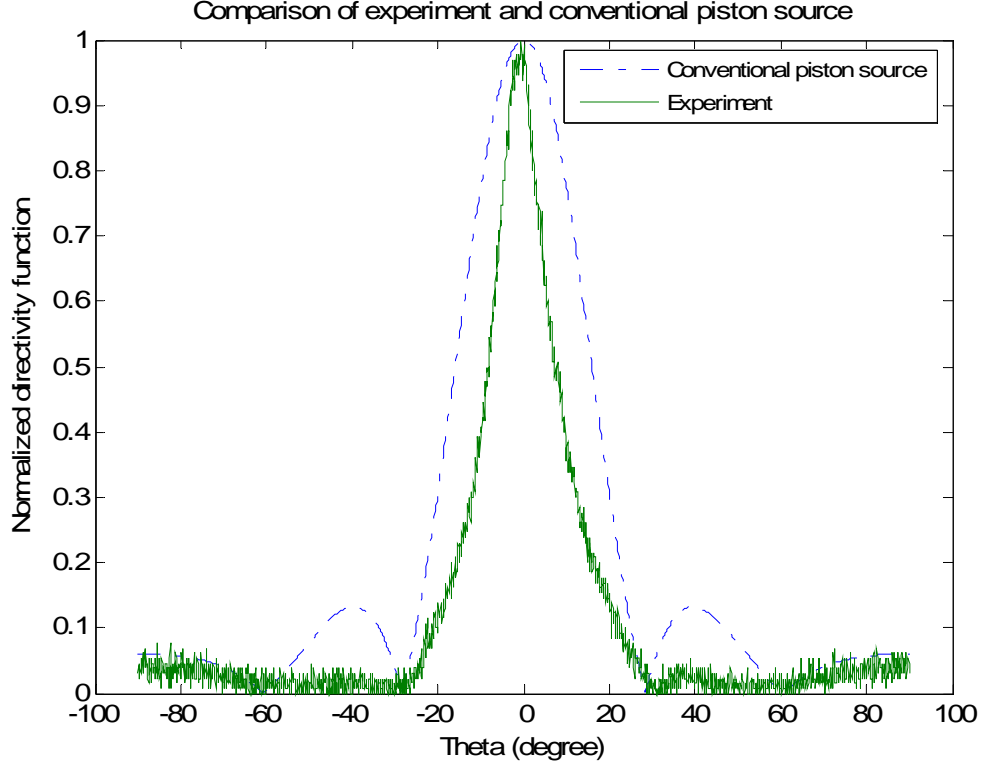
Figure 32.   Comparison of the experiment and conventional piston source.

B.   RANGE DEPENDENCE OF PRIMARY WAVES

The Holosonic parametric array that used in this experiment is a circular disk, containing an unknown number of small transducer elements. However, if we assume the parametric array to be a perfect circular piston source, the boundary of the far field region can be computed from

$$d = \frac{\pi a^2}{\lambda}$$
(3.6)

This distance is called Rayleigh distance (Kinsler et al., 2000). Within the near field region, the radiation pattern of any circular piston source shows strong interference effects on the axis of the aperture, hence we are expecting the radiation pattern of the parametric array to be quite complicated for the primary waves. Taking the mean value of the frequencies 59-61 kHz, the distance to the boundary where near field region of the parametric array ends is found to be 26.59 m, for a circular of radius of 0.22 m.

49

Therefore, we are confined to the near field of the parametric array due to the space limitation of the anechoic room used in this experiment.

In order to measure the high frequency field, a ¼" B&K 4136 microphone was used, because of its wide frequency response. Furthermore, the ½" microphone has a 3 dB high frequency roll-off at 20 kHz.   To measure the range of the primary signal, the microphone was aligned with the axis of the parametric array, where the farthest data point was taken at a distance of 4 m from the parametric array while the nearest data point was at 0.15 m. The experimental arrangement is the same as that in Fig. 29, with the exception that the elliptical filter, rms-dc converter and oscilloscope are replaced with a SR 785 dynamic signal analyzer.

The range dependence of the primary waves is shown in Fig. 33.
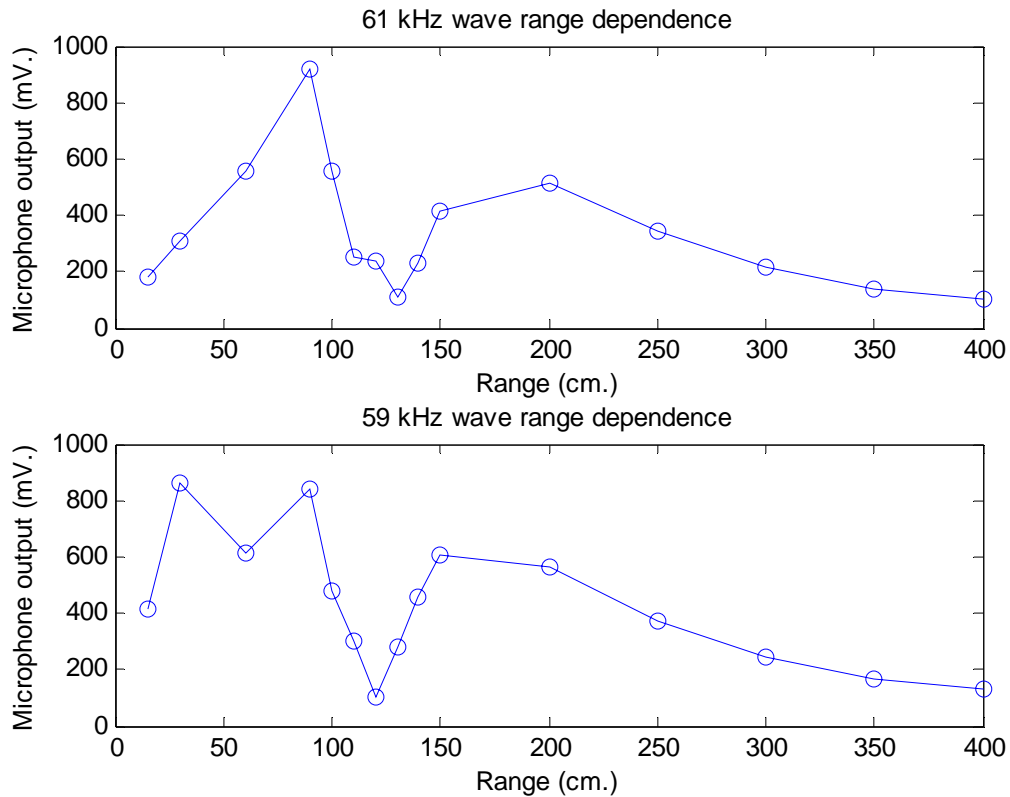
Figure 33.   Range dependence of the primary waves.

The fluctuations of the primary waves in the near field of the parametric array shown in Fig. 33 are expected. Theoretical near field axial pressure response for a baffled piston source for 59 kHz and 61 kHz primary waves are seen in Fig. 34. The near field of the ultrasonic waves is varying so fast that it does not seem possible to compare the theoretical plots with the experimental data, because the later is very sparse compared with the variations predicted by theory. Note that according to theory, within a distance of one meter of the parametric array, the pressure maxima and minima occur several tens of times. Furthermore, since the wavelength of the primary waves are so small (0.57 cm), being on–axis of the parametric array is very difficult. Thus, we can conclude that it is not reasonable to compare the experimental data with theoretical near field behavior of the piston source for the primary waves.

Figure 34. Axial response of the piston source that operates at 59 kHz for the upper figure and 61 kHz for the lower figure in the near field region.

C.   RANGE DEPENDENCE OF DIFFERENCE WAVE

Difference wave generation takes place along the interaction length due to the nonlinear interaction of the primary waves. If we assume that along the interaction length the primary waves are highly collimated, then the difference frequency is confined to the geometry of the source. Because of their high frequency, primary waves do not spread propagating as plane waves within the near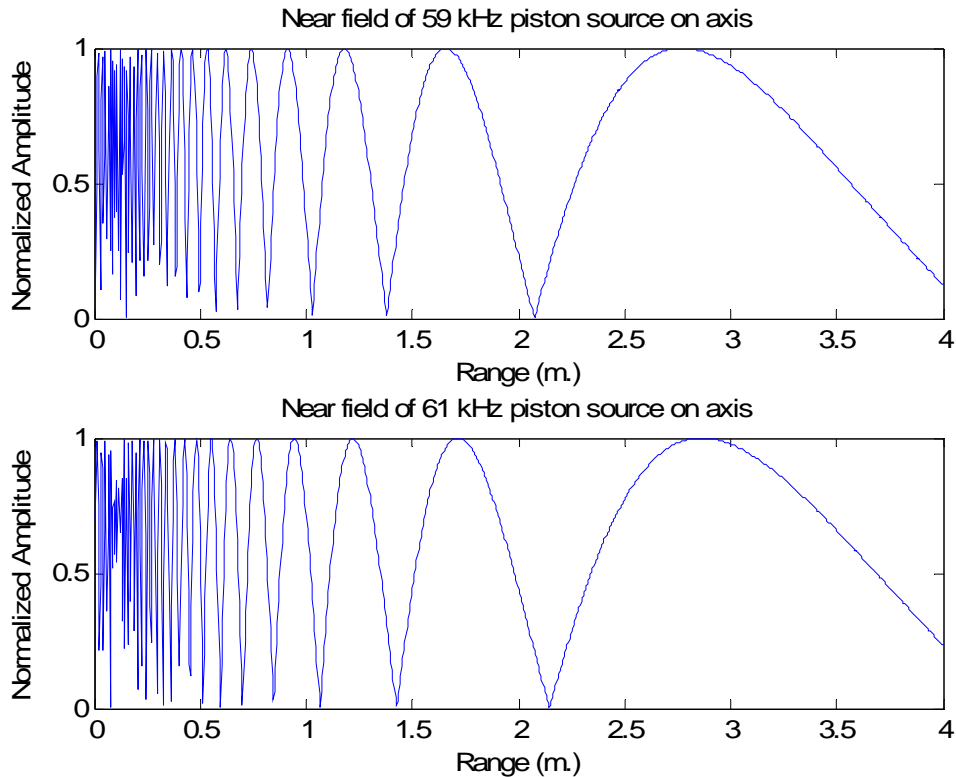 field. We observed in the experiment that spreading of the difference wave does not take place at the distance which is determined by Eq. (4.1) as the conventional piston source:

$$d = \frac{\pi a^2}{\lambda}.$$

We can conclude that the far field of the parametric array starts at the point where the difference wave starts to decay because of the spherical spreading. In the near field region, the difference wave grows linearly according to second order perturbation analysis.

A ½" microphone was preferred for this part of our experiment due to its high sensitivity (48.21 mV/Pa) and good bandwidth; the amplitude of the difference wave that is relatively weak compared to primary waves.

In order to compare the experimental data with the theory, we need to divide the theory into two parts. The first part yields the difference wave growth, while the second part is the attenuation of the wave due to the spreading. The spherical spreading is dominant over the attenuation mechanism of the wave. When absorption of difference wave in air is negligible, Equation (2.38) shows us the linear growth of the difference wave is given by

$$p_2 \;=\; -\frac{\beta P_0^{\,2}\omega_-}{2\rho_0 c_0^3}\,x\Big[\,\sin\big(\omega_- t - k_- x\big)\Big].$$

After the difference wave production terminates due to absorption of the high frequency primary waves, the difference wave attenuates proportional to *1/R* because of the spherical spreading. Therefore, we need to incorporate two regions in order to be able to

show wave generation and attenuation due to spreading. In the theoretical plot, first, the difference wave will grow until the maximum experimental data point, and after that point, it will decrease as *1/R*. The comparison of the experimental data and the theory is shown in Figure 35.
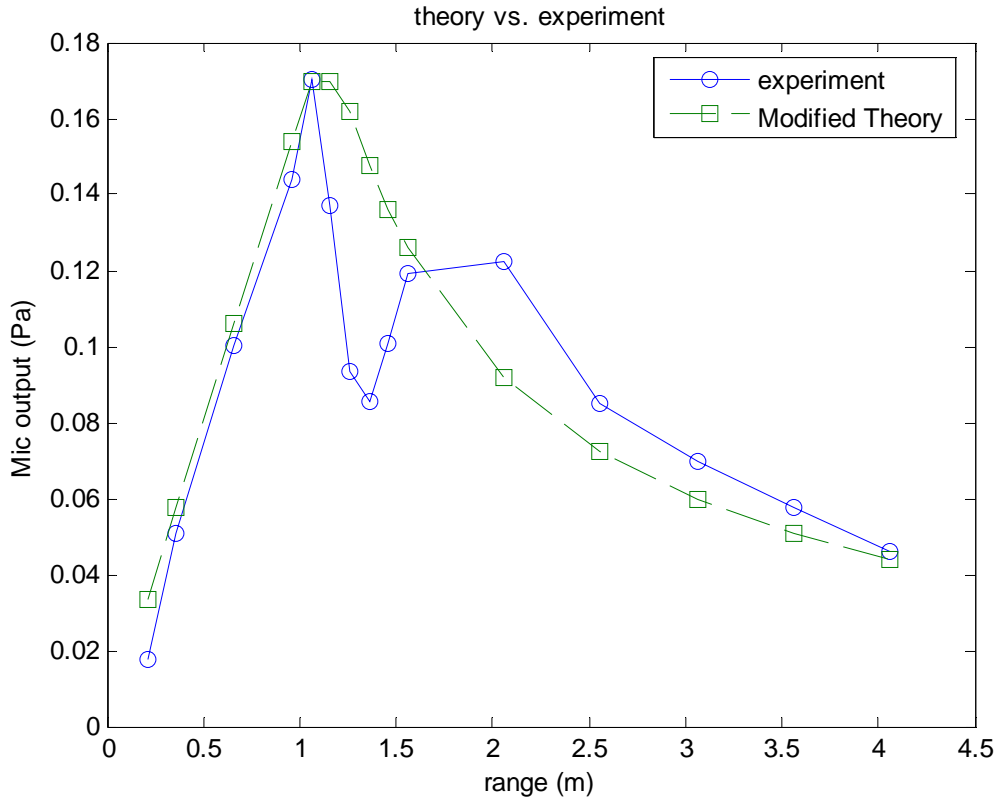
Figure 35.   Comparison of the experimental data of 2 kHz difference wave for range
dependence measurements with the theory.

The first part of the graph showing linear growth of the difference wave is in good agreement with the theory. The generation of the difference wave takes place along a distance of about 1.2 m of the parametric array. We can specify this distance as the far field boundary of the parametric array. After the sound pressure reaches its maximum point, the sound wave starts to spread as expected. That marks the transition to the far field of the parametric array. At a distance of about 4 m, the theory and the experimental values have a close agreement. That is because of the interference effects of the primary waves have diminished with distance from the parametric array.

D. TOTAL HARMONIC DISTORTION (THD) MEASUREMENTS

"For total harmonic distortion, one needs to include the sum of RMS square of all harmonics as a percentage compared to the amplitude square of the fundamental signal. Square root of this expression which is used commonly in audio applications yields the total harmonic distortion" (http://zone.ni.com/devzone/cda/tut/p/id/2120):

$$THD = \sqrt{\frac{V_2^2 + V_3^2 + V_4^2 + ... + V_n^2}{V_1^2}} \times 100. \tag{3.7}$$

Harmonic distortion is an important issue in parametric arrays because a nonlinearly produced difference wave and its harmonics can cause high harmonic distortion levels of the intended demodulation. This prevents the reproduction of a clean, high fidelity audio signal. The parametric array which we have used in the experiment comes with a pre-amplifier that preprocesses the audio signal to eliminate the harmonic distortion. This audio signal amplitude modulates the ultrasonic signal. According to the theory (Yoneyama et al., 1983), a DSBAM-WC (double side band amplitude modulation with carrier) technique should be used in the amplitude modulation process, because without carrier frequency, a harmonic of the audio signal is produced in the air, which is not desirable in audio applications of the parametric array. Even though harmonic distortion is severe with the DSBAM-WC compared to DSBAM-SC, we are going to use this amplitude modulation technique in the harmonic distortion measurements. The upper plot in Figure 36 which shows the response of DSBAM-WC has clearly higher harmonic distortion compared to lower figure which shows the response of DSBAM-SC.

As shown in the figure, the second harmonic of the 2 kHz difference frequency wave, which is the result of interaction of the sidebands, is strong. In order to fully quantify the THD, we first perform the measurements without using the pre-amplifier. In this case, we are able to see the real harmonic distortion produced by the parametric array. We then follow this with a measurement that allows us to investigate the relation between the modulation depth and harmonic distortion. As we have seen in the theory (Chapter II), decreasing the modulation depth will decrease the distortion at the expense of the difference wave output. Consequently, we will also look at the response of

decreasing modulation depth to the signal output. Finally, we observe the effects of the high frequency leveling, low frequency cut-off and volume control knobs on the harmonic distortion of the parametric array.
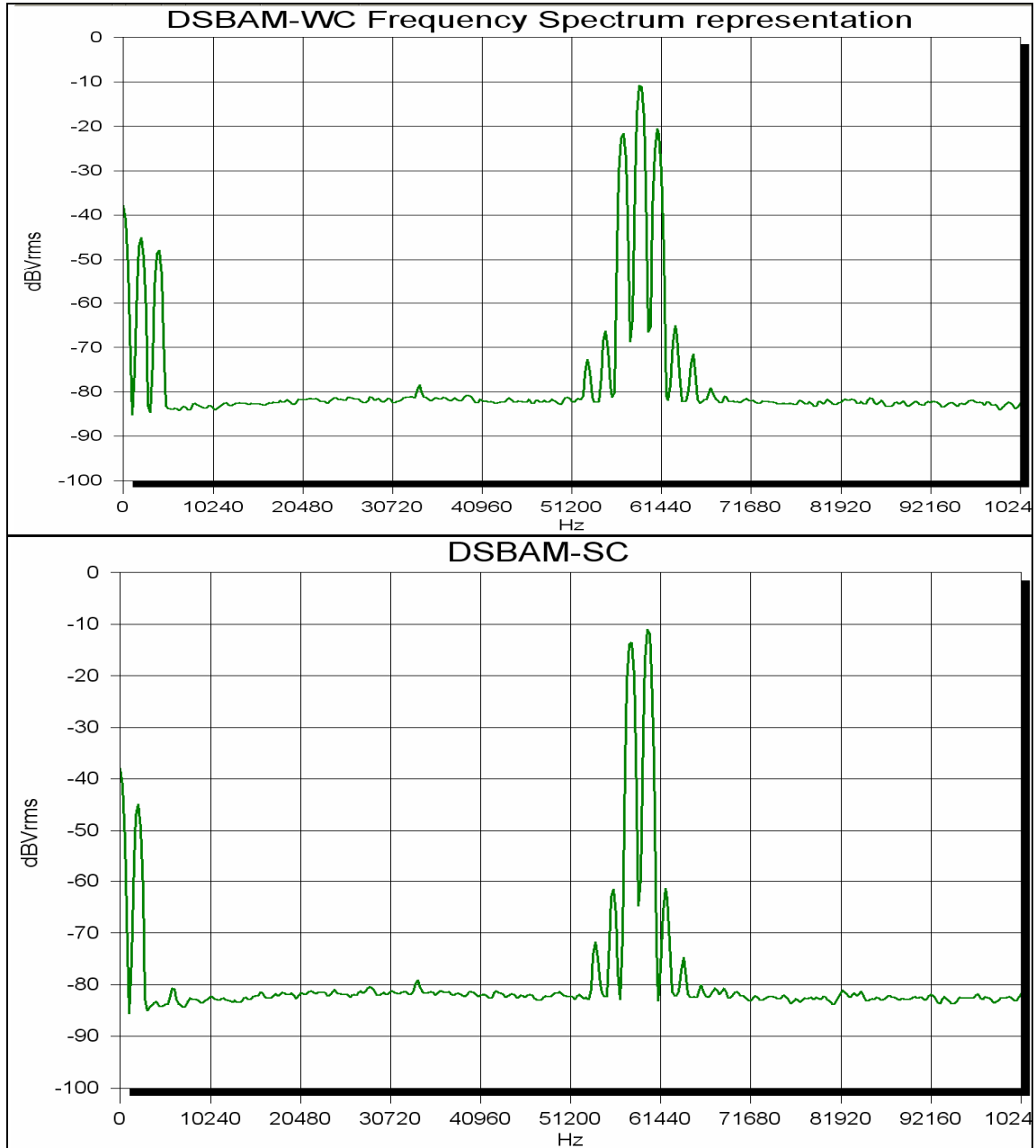
Figure 36.　Frequency spectrum of the parametric array. The upper figure shows the frequency spectrum of 59 kHz primary wave amplitude modulated by 2 kHz audio signal with the carrier frequency, while the lower figure is modulation without the carrier frequency.

Figure 37 shows the relation between the modulation depth and harmonic distortion. As expected, harmonic distortion should increase when the modulation depth increases. Figure 38 shows the microphone output vs. modulation depth.
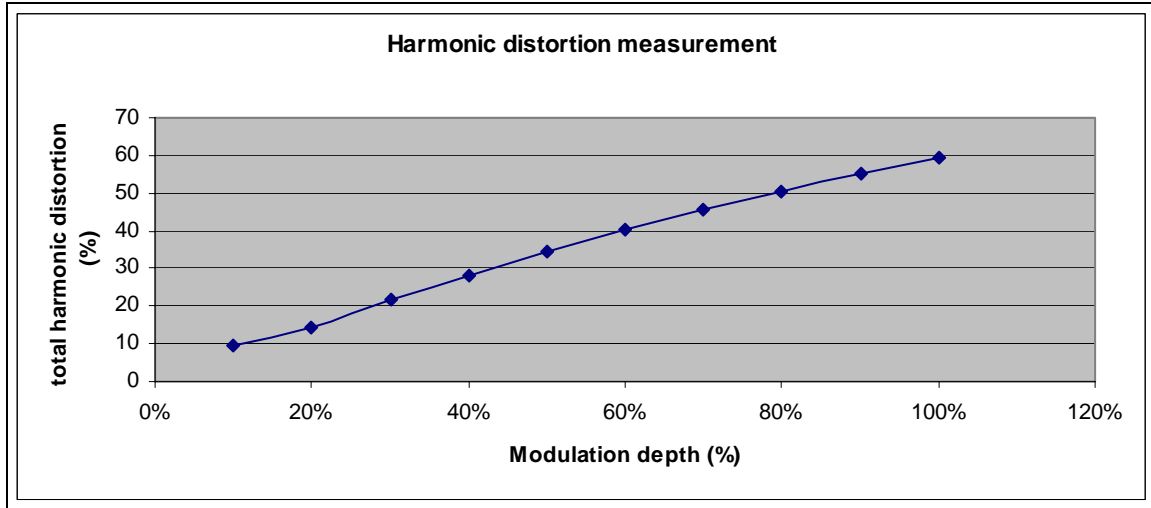
Figure 37.   Total harmonic distortion of the parametric array vs. modulation depth.
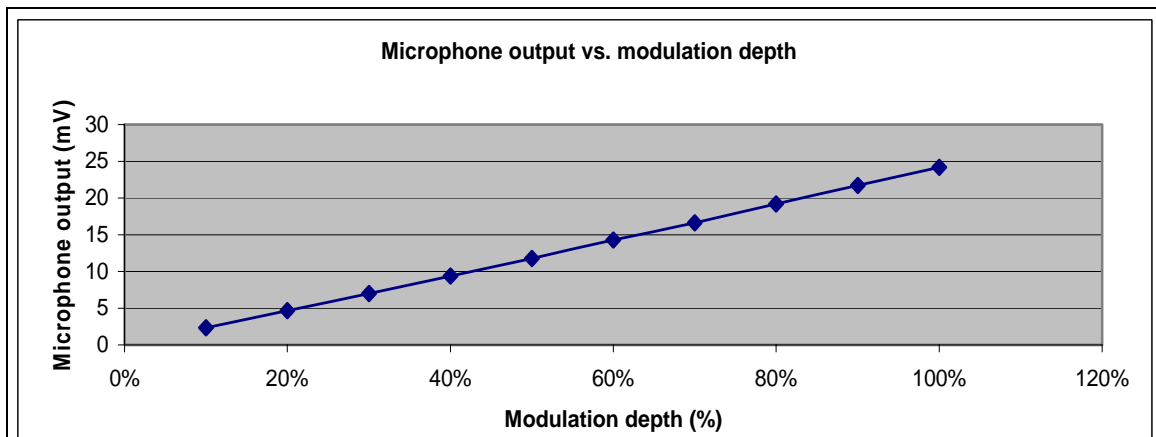
Figure 38.   Microphone output vs. modulation depth.

In these experiments a 59 kHz signal was used as a primary wave, modulated by a 2 kHz signal as the difference wave. A ½" microphone was used as the receiver with a preamplifier gain of 20. The signal picked by microphone was sent to preamplifier before reaching signal analyzer. The gain of the preamplifier is adjusted to ten.

Without using the preprocessing amplifier, the THD yields a highly distorted signal. In order to see the effectiveness of the preprocessing amplifier, we connected the amplifier and preprocessed the signal before sending it to the parametric array. Total harmonic distortion was reduced to 3.9 % from 59.3 %. This value is sufficient for clean audio signal reproduction.

As a final step in the experiment, we have investigated the functionality of the knobs on the pre-amplifier. There are three knobs in front of the pre-amplifier which can only be controlled in the audio mode of the parametric array (Figure 39)

Figure 39.   Pre-amplifier of Holosonic's parametric array.

The volume knob simply controls the amplitude of the signal. "Low Freq" and "High Freq" knobs operate just like a filter. The Low Freq knob filters the low frequency component of the signal while the High Freq knob filters the high frequencies. The effects of these knobs on harmonic distortion are summarized in Table 2. For each knob, three different values are taken when the knob is at its max point, half way, and at the min point.

Low frequency cut-off knob (THD %)		High frequency cut-off knob (THD %)	
Min	3.9	Min	3.9
Half way	5.33	Half	4.68
Max	5.55	Max	10.1

Table 2.   The Harmonic distortion measurements for the control knobs on the Holosonic's pre-amplifier.

THIS PAGE INTENTIONALLY LEFT BLANK

V.   CONCLUSIONS AND FUTURE WORK

In Chapter III of the thesis, the nonlinear end-fired parametric array was modeled using linear point sources. An exponential tapering was applied to the each element that made up the linear end-fired array. Our model can be thought as a continuous line source because the spacing between the source elements was about 0.3 cm. The length of the array for the model was determined according to the interaction length. Two different interaction lengths were used in the model. The first interaction length, which we calculated from $L=1/2\alpha$, was about 2.9 m. Originally, it was expected that the linear model would mimic the nonlinear end-fired parametric array. However, for this interaction length our linear model did not yield the expected high directivity and side lobe free beam pattern. Therefore, we decided to increase the interaction length to $L=4/\alpha$, which is about 23.2 m. The results showed good agreement between the linear model and the theoretical Westervelt directivity function in terms of the beam pattern for parametric array. The negative results for the shorter interaction length might be due to the assumptions that we had made in the model, where we assumed that the interaction of ultrasonic sound waves took place only at the axis of the source. Based on this assumption, we constructed the linear array model as a line source. But interaction occurs within the volume bounded by the parametric array source. Therefore, for a future work, a linear volumetric array can be modeled and we believe that it would give better results in terms of directivity and side lobes for shorter interaction lengths.

In Chapter IV, experimental results were presented. The parametric array which we used in the experiment was the AS-18-B audio spotlight from Holosonic Company. The experiments were conducted in the anechoic room in order to minimize the reflections from the boundaries. Because the anechoic room is of limited space, we were restricted to the near field of the parametric array. Theoretical calculations that were made for comparison purposes are based on the far field approximation.

Beam patterns of the generated difference wave frequency signal were plotted (Figure 30, Figure 31). It was seen that parametric array had quite narrow beam width and almost no side lobes, in agreement with Westervelt's theory (Figure 32).

59

For measurements of range dependence of the signals, both the primary waves and the difference wave frequency signal were examined. Due to the complicated interference of the primary waves, it was not possible to compare the theory and the experiment.

The range measurements for the difference frequency signal, were fitted with two asymptotical behaviors, one dealing with nonlinear generation and growth of the difference wave as a one-dimensional process, and the other dealing with the further evolution of the difference waves due to spherical spreading. The two asymptotic behaviors were matched at the point where the wave generation terminates at a maximum, which is assumed the point where spherical spreading starts. This modified theoretical response of the parametric array for the difference wave frequency signal showed reasonable agreement with the experimental data (Figure 35). Significant agreement in the first region (wave generation) was shown by the data. In the second region, theory and experiment agree with increasing distance.

We observed that total harmonic distortion (THD) was severe for the parametric array unless we used the pre-processing amplifier. It was shown that harmonic distortion depends on modulation depth (Figure 37). However, according to the Yoneyama et al. (1983), we were expecting the m^2 dependence between the harmonic distortion and the modulation depth. But, it seemed that there was more like a linear dependence between them. Finally, we have seen that the pre-processing amplifier, which pre-distorts the audio signal is really needed for a clean signal reproduction, because preprocessing has reduced the total harmonic distortion from 59.3 % to about 3.9 %.

Thus, future research may be carried out to design a parametric array for the purpose of investigating the dependence on geometry and components of the array on the beam directivity. This may provide more control in the experiment such as operating frequency of the array elements and array size which would change the far field distance of the parametric array. It is very important that the experiment should be performed in the far field because all of the theoretical predictions are based on the far field of the parametric array.

Finally, there will be some experiments conducted by LT Noble Hetherington USN and LT Richard Pratt USN in their thesis that will investigate the possible applications of the parametric array in wake detection and tracking.

THIS PAGE INTENTIONALLY LEFT BLANK

LIST OF REFERENCES

Atchley, A. A. (2005, October). Not Your Ordinary Sound Experience: A Nonlinear-Acoustic Primer. *Acoustics Today*, 1, 19-24.

Barnard, G. R., Willette, J. G., Truchard, J. J., & Shooter, J. A. (1972). Parametric Acoustic Receiving Array. *J. Acoust. Soc. Am.*, 52, 1437-1441.

Bass, H. E., Bauer, H. J., & Evans, L. B. (1972). Atmospheric Absorption of Sound: Analytical Expressions. *J. Acoust. Soc. Am.*, 52, 821-825.

Bellin, J. L. S., & Beyer, R. T. (1960). Scattering of Sound by Sound. *J. Acoust. Soc. Am.*, 32, 339-341.

Bellin, J. L. S. & Beyer, R. T. (2000). Experimental Investigation of an End-fired Array. *The J. Acoust. Soc. Am.*, 34, 1051-1054.

Bennett, M. B. & Blackstock, D. T. (1975). Parametric Array in Air. *J. Acoust. Soc. Am.*, 57, 562-568.

Berktay, H. O. (1965). Possible Exploitation of Non-Linear Acoustics in Underwater Transmitting Applications. *J. Sound and Vib.*, 2, 435-461.

Berktay, H. O., & Muir, T. G. (1973). Arrays of Parametric Receiving Arrays. *J. Acoust. Soc. Am.*, 53, 1377-1383.

Denardo, B. C. & Larraza, A. (2006). Notes for PH 4459 (*Nonlinear Oscillations and Waves*). Naval Postgraduate School, Monterey, California: (unpublished).

Hines, P. C., Risley, W. C., & O'Connor, M. P. (1998). A Wide-Band Sonar for Underwater Acoustics Measurements in Shallow Water. *Proc. of Ocean's 98 Conf.*, IEEE Press, 1558-1562, 3, Nice.

Kinsler, L. E., Frey, A. R., Coppens, A. B., & Sanders, J. V. (2000). *Fundamentals of Acoustics Fourth Edition*, USA, John Wiley & Sons Inc.

Kite, T., Post, J. T., Hamilton, M. F. (1998). Parametric Array in Air: Distortion Reduction by Preprocessing. *in Proc. 16th Int. Cong. Acoust.*, 2 , 1091-1092.

Konrad, W. L., & Navin, J. G. (1973). Investigation of the Parametric Radiator as a Wide-Band Calibrator Source. *J. Acoust. Soc. Am.*, 53, 383.

Mcclellan, J. H., Schafer, R. W., & Yoder, M. A. (2003). *Signal Processing First*, NJ, Pearson Prentice Hall.

Muir, T. G., & Wyber, R. J. (1984). High Resolution Seismic Profiling with a Low-Frequency Parametric Array. *J. Acoust. Soc. Am.*, 76, 78.

National Instruments NI Developer Zone. Total Harmonic Distortion. Retrieved January 4, 2007, from http://zone.ni.com/devzone/cda/tut/p/id/2120

Naugolnykh, K. & Ostrovsky, L. (1998). Parametric Acoustic Transmitters. in *Nonlinear Wave Processes in Acoustics*, 186-188, New York, Cambridge University Press.

Pompei, F. J. (1999). The Use of Airborne Ultrasonics for Generating Audible Sound Beams. *J. Aud. Eng. Soc.*, 47, 726-731.

Vyas, A. L., Raj, V. S. B., Gupta, R. G. (1998). Design Considerations of Parametric Arrays. *Underwater Technology Proceedings of the 1998 International Symposium on,* 98-102.

Westervelt, P. J. (1957). Scattering of Sound by Sound. J. Acoust. Soc. Am., 29, 199-203.

Westervelt, P. J. (1963). Parametric Acoustic Array. *J. Acoust. Soc. Am.,* 35, 535-537.

Yoneyama, M., Fujimoto, J., Kawamo, Y., & Sasabe, S. (1983). The Audio Spotlight: An application of nonlinear interaction of sound waves to a new type of loudspeaker design *J. Acoust. Soc. Am.,* 73, 1532-1536.

Wijk, K. V., Scales, J. A., Mikesell, T. D., & Peacock, J. R. (2005). Toward Noncontacting Seismology. *Geophys. Res. Let.*, 32, L01308.

INITIAL DISTRIBUTION LIST

1.   Defense Technical Information Center
        Ft. Belvoir, Virginia

2.   Dudley Knox Library
        Naval Postgraduate School
        Monterey, California

3.   Physics Department
        Naval Post Graduate School
        Monterey, California

4.   Professor Bruce C. Denardo
        Department of Physics
        Naval Post Graduate School
        Monterey, California

5.   Professor Andrés Larraza
        Department of Physics
        Naval Post Graduate School
        Monterey, California

6.   Professor Daphne Kapolka
        Department of Physics
        Naval Post Graduate School
        Monterey, California

7.   Professor Kevin B. Smith
        Department of Physics
        Naval Post Graduate School
        Monterey, California

8.   Arastirma Merkezi Komutanligi (Turkish Naval Research Center Command)
        Turkish Navy
        Istanbul, Turkey

9.   Deniz Harp Okulu Komutanligi (Turkish Naval Academy)
        Turkish Navy
        Istanbul, Turkey